

# Inertial Measurement via Dynamics of Trapped Particles

by

Ernest Rehmatulla Post

M.S. Media Arts and Sciences, 1999  
Massachusetts Institute of Technology

B.S. Physics, 1996  
University of Massachusetts, Amherst

Submitted to the Program in Media Arts and Sciences,  
School of Architecture and Planning,  
in partial fulfillment of the requirements for  
the Degree of

Doctor of Philosophy  
at the Massachusetts Institute of Technology

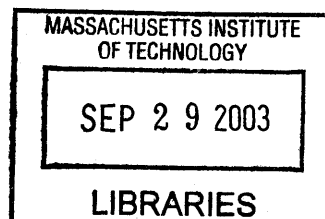
September 2003

© 2003 Massachusetts Institute of Technology  
All rights reserved

Signature of Author: \_\_\_\_\_  
Program in Media Arts and Sciences  
August 22, 2003

Certified by: \_\_\_\_\_  
Neil A. Gershenfeld  
Director, Center for Bits and Atoms  
Thesis Supervisor

Accepted by: \_\_\_\_\_  
Andrew Lippman  
Chairperson, Department Committee on Graduate Students



ROTCH



# Inertial Measurement via Dynamics of Trapped Particles

by

Ernest Rehmatulla Post

Submitted to the Program in Media Arts and Sciences,  
School of Architecture and Planning,  
on August 8, 2003  
in partial fulfillment of the requirements for  
the Degree of

Doctor of Philosophy  
at the Massachusetts Institute of Technology

## Abstract

We describe theoretical and practical aspects of the particle trap as an inertial sensor. The insight motivating this approach is that a trapped particle acts like a mass on a spring, but the restoring forces are provided by electrostatic fields. Exquisitely machined physical mechanisms can be replaced by carefully tuned mechanical physics. Such inertial sensors could be simpler to build yet exhibit superior performance because their operating parameters can be dynamically controlled.

Most currently available inertial sensors are inherently planar devices that obtain no more than two degrees of motional sensitivity from a given proof mass. The availability of an accurate, inexpensive, integrated six-degree-of-freedom inertial sensor would enable new applications of inertial sensing that are presently either infeasible or unconsidered.

By adding inertial terms to the Paul trap dynamics we derive classical observables that depend on the local acceleration field. We also confirm that these observables appear in practice, in what we believe to be the first electrodynamic particle trap accelerometer. An important (and unusual) aspect of our accelerometer is its dynamic tunability: its effective spring constant depends on the trap drive parameters. Our roughly constructed trap also exhibits a large region of linear response to acceleration, and we present evidence suggesting that our accelerometer has performance comparable to commercially available sensors.

Thesis Supervisor: Neil A. Gershenfeld  
Title: Professor of Media Arts and Sciences  
Director, MIT Center for Bits and Atoms



# Inertial Measurement via Dynamics of Trapped Particles


by


Ernest Rehmatulla Post


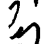
Submitted to the Program in Media Arts and Sciences,  
School of Architecture and Planning,  
in partial fulfillment of the requirements for  
the Degree of

Doctor of Philosophy  
at the Massachusetts Institute of Technology

August 2003

Thesis Supervisor  Neil A. Gershenfeld  
Professor of Media Arts and Sciences  
Director, MIT Center for Bits and Atoms

Thesis Reader  Joseph A. Paradiso  
Associate Professor of Media Arts and Sciences  
MIT Media Laboratory

Thesis Reader   Scott R. Manalis  
Associate Professor of Media Arts and Sciences  
MIT Media Laboratory



## Acknowledgments

We are all instruments of our social context; accordingly, this work is dedicated to the many who have shared with me their wisdom, enterprise, and humanity. I beg the reader's patience with this exhaustive yet incomplete list.

Of my mentors at the Media Lab I am incredibly grateful to Neil Gershenfeld, for always finding time to work with his students and encouraging their (and his!) crazy ideas, even as he built our little physics lab into the Center for Bits and Atoms; Susan Murphy-Bottari, for making our group feel like family and run like Swiss clockwork, along with the help of Mike Houlihan; Joe Paradiso for his quiet wisdom, his offhanded deep insights into physics, and his passion for electronic music; and Scott Manalis for his clear sight and carefully calibrated challenges. I must also thank Sandy Pentland, Roz Picard, Joe Jacobson, Mike Hawley, Hiroshi Ishii, and John Maeda.

Throughout my seven years at the Media Lab, I am honored to have been both an Interval Research Fellow and a Motorola Fellow. I am also grateful to the Center for Bits and Atoms for their support of this work under NSF Grant CCR-0122419.

There are my many colleagues in the Bits and Atoms family: Matt Reynolds, Bernd Schoner, Yael Maguire, Ravi Pappu, Ben Recht, Jason Taylor, Raffi Krikorian, Manu Prakash, Bill Butera, Saul Griffith, James McBride, Vikas Anant, Dave Mosley, Brian Chow, John-Paul Strachan, Matt Hancher, Rich Fletcher, Ben Vigoda, Olufemi Omojola, Josh Smith, Babak Nivi, and Edward Boyden to name a few. It's been quite a ride.

Around the lab, it has been a pleasure to work and play with Wendy Ju, Rob Poor, Maggie Orth, Emily Cooper, Peter Russo, Kwin Kramer, Rick Borovoy, Joe Pompei, Brygg Ullmer, Bakhtiar Mikhak, Chris Lyons, Limor Fried, and especially Kelly Dobson and Diana Young.

In my borg days, I enjoyed being assimilated by Thad Starner, Lenny Foner, Brad Rhodes, Josh Weaver, Dana Kirsch, Steve Mann, and the itinerant Joost Bonsen.

No Media Lab thesis would ever come to term without Linda Peterson's tough love for the students in her charge, and of her many able assistants past and present I am particularly indebted to Santana Tonelli and Pat Solakoff. In the ongoing theater of academic presentations, Matt Tragert always gives generously of himself to ensure that the show goes on smoothly.

Of many others who have taught me important lessons in life, I will always remember: Beatrice Domanski, Joy Odom, Charles Rieger, Randy Trigg, Andrew Beals, Chris Torek, Fred Blonder, Charles Adler, Don Hopkins, James O'Toole, Michelle McElvany, Mike Gallaher, Liz Sommers, Sarah T. C. Kaye, John Romkey, James van Bokkelen, Margaret Wasserman, Steve Wadlow, H. Shrikumar, John Brehm, Sam Holland, Mark Tuominen, Eugene Golowich, Andy Barto, Rob Gramer, Julia Tenney, Kit Waal, and of course Mark Weiser, for taking me under his wing and teaching me how to C by leaving a trail of cryptic comments in Unix kernel source code.

To Edward and Zehra Post, for bringing me into this world, hooking me on phonics, and teaching me to use a slide rule, and to my brother Burton for his admiration.

And to Jenny Gutbezahl, for sharing her life, love, and brilliance with me – thank you so much.





# Table of contents

<b>1 Introduction</b>	11
1.1 Overview	11
1.1.1 Introduction	11
1.1.2 Inertial user interfaces	11
1.1.3 Inertial effects in particle traps	12
1.1.4 Experimental methods	13
1.1.5 Results	14
1.1.6 Discussion	14
<b>2 Inertial user interfaces</b>	15
2.1 Black-box inertial navigation	16
2.2 An exemplary pointing device	16
2.3 Inertial sensing of human motion	17
2.4 Inertial interface regimes	18
2.5 Generalized surface inertial channel	19
2.6 Inertial actuation	21
2.7 A “hopping” actuator	21
2.8 A hopping kinetic display	21
2.9 The INERTIAL FRAME	22

<b>3 Inertial effects in particle traps</b> . . . . .	25
3.1 The particle trap as accelerometer . . . . .	25
3.2 Derivation of the pseudopotential . . . . .	29
3.3 Inertial signature in trap dynamics . . . . .	31
3.4 Geometry of a 3-symmetric inertial measurement trap . . . . .	32
3.5 Accelerometer noise models . . . . .	35
<b>4 Experimental methods</b> . . . . .	37
4.1 Simulation of an inertial measurement trap . . . . .	37
4.2 Physical realization of Paul traps . . . . .	40
4.3 Developing a practical trap . . . . .	43
4.3.1 Planar traps . . . . .	44
4.3.2 Trap loading . . . . .	46
4.3.3 Planar trap construction . . . . .	48
4.3.4 Particle tracking and readout . . . . .	49
4.4 Experimental configurations . . . . .	50
<b>5 Results</b> . . . . .	55
5.1 Experimental protocol . . . . .	56
5.2 Calibration . . . . .	58
5.3 Tunability . . . . .	59
5.4 Drift . . . . .	61
5.5 Noise power spectral density . . . . .	62
<b>6 Discussion</b> . . . . .	65
6.1 Future work . . . . .	65
<b>Bibliography</b> . . . . .	69

# Chapter 1

## Introduction

This dissertation explores the use of particle traps as inertial sensors. The insight motivating this approach is that a trapped particle acts like a mass on a spring, but the restoring forces are provided by electrostatics. Exquisitely machined physical mechanisms can be replaced by carefully tuned mechanical physics. Such inertial sensors could be simpler to build yet exhibit superior performance because their operating parameters can be dynamically controlled.

### 1.1 Overview

Without further ado, here is an outline of the present document.

#### 1.1.1 Introduction

This chapter provides an overview of the methods and motives that have driven the present work.

#### 1.1.2 Inertial user interfaces

Why is this thesis concerned with the problem of inertial measurement? The problem is stated clearly, by providing context to expose its relevance and impose constraints upon its solution.

An accelerometer can be most simply described as a mass on a spring, at equilibrium with the local acceleration field, along with some means to read out the equilibrium position and thence infer the applied acceleration. In fact, this model of an accelerometer will suffice for most of the exposition to follow.

For many years the market for inertial measurement was restricted to defense and aerospace applications; accordingly, devices were optimized for high accuracy and low bias, while volumes remained low, prices and complexity high. The first accurate, mass-manufactured accelerometers were MEMS devices that found application as automotive collision detectors. Since then, new applications and markets have begun to emerge, but at this writing none yet have a volume comparable to that of the automotive niche. One might reasonably argue that these applications have not yet emerged because available inertial sensors still do not meet niche requirements in terms of price per degree of freedom, physical sensor size, sensitivity, bandwidth, and drift, to name the most critical parameters.

Particle traps are key to many of today's most sensitive and accurate metrological techniques. They are commonly used as mass balances and spectrometers, but also provide the isolation and control necessary to manipulate atoms, ions, and electrons singly and stably for arbitrarily long intervals. The overarching, long-term goal of this work is to dynamically construct micron-scale electromechanical structures in traps and to stabilize them against inertial effects. As a beneficial side-effect, we show in this thesis how to use suspended structures as inertial sensors.

### 1.1.3 Inertial effects in particle traps

To use a particle trap as an inertial sensor it is necessary to determine how the trap dynamics depend on inertial perturbations. To a surprising degree, trapped particles can be considered to be elastically constrained to a point by an effective linear restoring force.

As with any approximation, several caveats pertain. The guiding fields of an electrodynamic trap cannot have arbitrary geometries, as Maxwell's equations disallow free-standing, static electric potential minima. While it is not possible to create a static potential that acts like a spring, it is possible to create a time-dependent potential that focuses charged particles to stable equilibria.

The end effect is that particles can be stably constrained to a fixed coordinate based on their charge and mass as well as the spectrum of guiding fields applied to the trap. Furthermore, the zones of stability in parameter space are effectively widened when a trap operates in a dissipative regime.

A useful approximation is the pseudopotential, an effective potential that arises as the time-averaged effect of the trap electric potential acting on a charged particle. The pseudopotential is overwhelmingly quadratic: trap symmetries allow only even-order terms, while electrostatics tends to smooth out any higher-order features. Using the pseudopotential, we derive the effects of inertial signals upon the system, showing distinct channels for the proportional readout of applied acceleration, both in a particle's center of motion as well as its amplitude of motion, and that these readout are decoupled for each spatial degree of freedom.

#### 1.1.4 Experimental methods

The presence of inertial readout channels is first confirmed through numerical experiments that simulate the dynamics of a Paul trap in an inertial field. Unfortunately, the ideal hyperboloidal geometry of the Paul trap poses challenges in fabrication, so through finite element modeling we greatly simplify the trap's electrode geometry while retaining the necessary field geometry, with the goal of realizing a planar structure. The planar geometry simplifies not only field modeling and fabrication, but also mounting and trap loading.

A practical, manufacturable sensor would use a simple, accurate readout technique such as optical interferometry, optical leverage, or resonant electric field absorption (to name the leading candidates). However, to allow flexibility in construction and characterization of our sensors, we use metrological techniques based on video microscopy and particle tracking by image processing.

Since the prototype accelerometers are large structures with many mechanical resonances, characterization is performed at known applied static accelerations by rotating the trap in the earth's gravitational field. To demonstrate the tunability of the trap, operating parameters such as guiding potential scale and frequency are also varied. Since the image of a particle on the sensor covers several pixels, particle positions may be determined to sub-pixel resolution by simple interpolation.

Although video microscopy affords a high pixel bandwidth (on the order of MHz), the temporal resolution of image features is limited to the frame rate (tens of Hz). While this does not greatly limit long-term drift or bias measurements, we would like to perform measurements of the noise spectral density over a wider band. Accordingly, a second experiment is devised to provide a readout of a particle's motional noise from the reflected intensity profile as it intersects the waist of a focused beam. The measurement is calibrated by the application of small static accelerations.

### 1.1.5 Results

From the characterization by video microscopy, we obtain calibration curves for trap sensitivity, as well as confirmation of readout linearity over a large range. This allows measurement of the effective spring constant and demonstration of its tunability as a function of trap operating parameters.

From the characterization by scalar intensity readout, we reveal interesting features in the noise spectrum that correspond to trap tuning and system thermalization and obtain an estimate of sensitivity.

### 1.1.6 Discussion

This thesis makes several contributions pertaining to the development of inertial sensors based on particle traps. It derives the inertial signature present in trap dynamics and demonstrates these effects by construction of a simplified 2-axis accelerometer with performance comparable to commodity sensors.

Having demonstrated the feasibility of this approach, we plot a course toward the realization of a practical sensor. We outline the work to come, focusing on issues of readout, realization of six-degree-of-freedom measurement, packaging, and economics.

## Chapter 2

# Inertial user interfaces

As inertial sensors improve in resolution and accuracy, new forms of inertial user interface will become possible. This paper seeks to first identify the pertinent performance metrics of inertial sensors likely to be found in tangible user interfaces, then bound their expected performance, and finally relate performance metrics to the gestural feature spaces they make accessible to the interface designer. This rough taxonomy is then used to sketch the INERTIAL FRAME, a proposed application for mediating interpersonal communication. It is the intent of this exercise to glimpse new modes of user interface that have been heretofore unconsidered.

It is probably safe to say that the measurement of position and orientation is central to the development of new forms of human-computer interfaces involving the manipulation of physical objects. Of the many ways to obtain these measurements, inertial sensing – *i.e.* the detection of changes in an object’s physical reference frame – stands out as the most autonomous. Indeed, the importance of inertially-informed UI has been noted since the earliest visions of Ubiquitous Computing [34].

In its most generic form, inertial sensing provides a foundation on which to develop tangible interfaces ranging from the personal to the architectural by providing certain unique capabilities, chief of which are a) the ability to function without a supporting infrastructure, b) a wide dynamic range, and c) broad frequency response.

In the present work, I aim first to provide a semi-rigorous introduction to the pertinent characteristics of inertial sensors and to identify the gestural feature spaces they make accessible to the interface designer. Then, by assuming sufficiently accurate sensors, I will consider some of the limits of tangible interfaces thereby enabled. Then I will consider the inverse problem of converting an inertial signal into motion and show how a free-standing object might obtain the ability to accelerate itself in an arbitrary direction. Finally, a proposed application that I call the INERTIAL FRAME shows how the foregoing pieces might fit together into a novel interpersonal haptic communicator.

The intent of this exercise is to sketch emerging sensing capabilities, to elucidate the parameters and limits of those capabilities, and to suggest ways in which designers can anticipate technological trends to develop new modes of inertial UI.

## 2.1 Black-box inertial navigation

The performance of an interface is ultimately determined by user testing in the intended application scenario rather than the specific technologies used in its implementation. If the interface design requires position information with a given resolution, this specification alone is insufficient to determine which spatial input scheme is the most applicable. Nonetheless, each position measurement technology imposes its own set of constraints.

One of these constraints is the need for an infrastructure. Many position measurement technologies require external references with well-known locations to establish a reference frame. Two examples of such systems are GPS on the global scale and Polhemus on the local scale. Although they can both be used to locate objects with millimeter precision, GPS requires said objects to be located outdoors within view of a constellation of signal source satellites (precluding indoor operation) while Polhemus requires objects to be located within a few meters of a reference antenna.

Inertial navigation on the other hand requires only that the local space-time continuum supports Newton’s laws of motion as embodied by the equation  $F = ma$ , which is to say that objects only change their motion in response to an applied force. There is good reason to believe that these laws hold universally, so the necessary infrastructure is already in place.

Inertial navigation has its own drawbacks, however, chief among which is the accumulation of error. When using an angular rate sensor, one may integrate the angular rate over time to determine orientation with the result that error accumulates linearly over time. Very accurate, affordable MEMS gyroscopes are on the horizon, with drift rates of tiny fractions of a degree per hour.

The situation is markedly worse when integrating a time-varying acceleration vector to obtain position, because as we shall see below, errors in acceleration accumulate quadratically over time. Of course, a multi-modal position sensing scheme will be better than one that relies solely on either inertial navigation or radiolocation, but a bound on the required performance of an inertial sensor can be obtained by considering the task of interest.

## 2.2 An exemplary pointing device

Suppose that we would like to build a general-purpose pointing device based entirely on inertial sensing, one that a user could simply pick up and point at objects in space, describe trajectories, or perhaps sketch or write on a surface. By first specifying its performance as seen by the user, we can then estimate its requisite inertial sensitivity by a quick calculation.

We can calculate a lower bound on the required inertial sensitivity by picking typical values based on experience. Suppose that a gestural “phrase” takes up to 10 seconds, requires a spatial resolution of 1 mm, and includes motional frequencies from 0 to 100 Hz.

From this rough specification we can determine the required noise and drift characteristics of the accelerometer. Position is obtained from acceleration by integrating twice

$$x = \int_0^T \int_0^T a \, dt^2 = \frac{1}{2} a t^2 \quad (2.1)$$



so the error  $\delta x$  in integrated position due to an error  $\delta a$  in measured acceleration is simply

$$\delta x = \frac{1}{2} t^2 \delta a . \quad (2.2)$$

The acceleration error  $\delta a$  itself can be determined from the average noise  $\eta$  present in the inertial signal and the signal's bandwidth

$$\delta a = \eta (\delta f)^2 . \quad (2.3)$$

Combining these to obtain a figure for the noise floor  $\eta$  yields

$$\eta = \frac{\delta a}{\sqrt{\delta f}} = \frac{2 \delta x}{t^2 \sqrt{\delta f}} . \quad (2.4)$$

In order to meet the specifications given above, the required sensor noise floor will be

$$\eta = \frac{2 (10^{-3} \text{ m})}{(10 \text{ s})^2 \sqrt{100 \text{ Hz}}} \frac{1 \text{ g}}{9.81 \text{ m s}^{-2}} \quad (2.5)$$

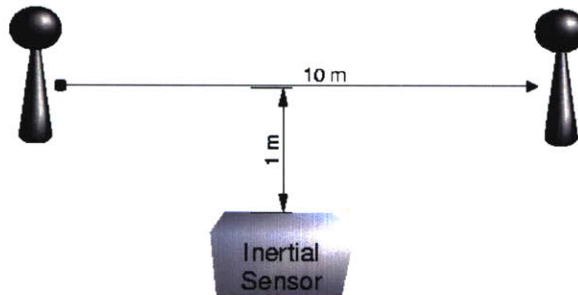
which corresponds to  $\eta = 2.038 \times 10^{-7} \text{ g}/\sqrt{\text{Hz}}$ . This level of performance lies somewhere between that of today's commercially available accelerometers and the most sensitive accelerometry techniques currently in practice [6].

The Analog Devices ADXL202 [1] is exemplary of commodity devices. It costs approximately \$15 US (in 2002) and has a maximum noise density of  $\eta = 10^{-3} \text{ g}/\sqrt{\text{Hz}}$ , and is currently one of the most popular devices among user interface designers and researchers [14].

## 2.3 Inertial sensing of human motion

How practical would it be to use inertial measurement to directly sense human beings and their transit through ambient media? In the next section a few calculations reveal the limiting capabilities of present practice in accelerometry.

Consider the transit of an adult human with a mass  $m=50 \text{ kg}$  past an inertial acceleration sensor, with a nearest approach of 1 m along a path 10 m long (as shown in Figure 2.1).



**Figure 2.1.** Path of human subject relative to a sensitive accelerometer.

Given the gravitational constant  $G = 6.672 \times 10^{-11} \text{m}^3 \text{kg}^{-1} \text{s}^{-2}$ , we find the acceleration due to the human (assuming a spherical human) to be

$$a = \frac{Gm}{r^2} \quad (2.6)$$

which varies from  $1.28 \times 10^{-10} \text{m s}^{-2}$  to  $3.33 \times 10^{-9} \text{m s}^{-2}$ , or from  $1.31 \times 10^{-11} \text{g}$  to  $3.40 \times 10^{-10} \text{g}$ . The only inertial sensor which presently admits this level of performance is the cold atom interferometer [6], which can resolve  $10^{-10} \text{g}$  (over an integration period of approximately 1 second).

Now consider the transit of a human hand with a mass  $m = 0.20 \text{kg}$  past an inertial acceleration sensor, with a nearest approach of 1 cm along a path 1 m long, as might be typical in a desktop user interface. By redoing the foregoing calculation with these parameters, we find the acceleration due to the hand at closest approach to be  $1.36 \times 10^{-8} \text{g}$ , a signal two orders of magnitude greater than the noise floor of the cold atom interferometer. This figure suggests future interfaces based upon direct measurement of the acceleration field due to a user's mass distribution. It also sets a benchmark for the sensitivity required to enable a new class of inertial user interfaces.

Note that accelerometric detection does not distinguish between individuals or objects; the pertinent characteristics are the objects' masses and motions. Signal amplitude will vary directly as the object's mass and inversely as the square of the object's distance. However, it may be possible to infer an object's identity from behavioral modeling or by using signal processing to detect characteristic motion signals.

## 2.4 Inertial interface regimes

The useful range of inertial effects in user interfaces extends roughly from the greatest accelerations that users are likely to generate or experience ( $10^2 \text{g}$ ) to the smallest effects they are likely to create directly ( $10^{-10} \text{g}$ ). Figure 2.2 depicts this range with existing or representative inertial sensors as well as classes of inertial effects in human motion and activity.

Large-magnitude effects are more familiar in the UI literature [32, 14] because of the availability of commercial devices sensitive in those regimes. The ADXL202 [1] is representative these devices.

The next lower regime is covered by the expected capabilities of interferometric MEMS accelerometers [7][22] developed at the MIT Media Lab. Applications in this regime involve the detection of surface acoustic waves [17, 25, 5] generated by user contact with a rigid, anchored surface.

The lowest regime on the graph indicates the limits set by the most sensitive accelerometers [6, 18, 2] available today. The corresponding application domain reflects the scale of accelerations due to human-scale masses.

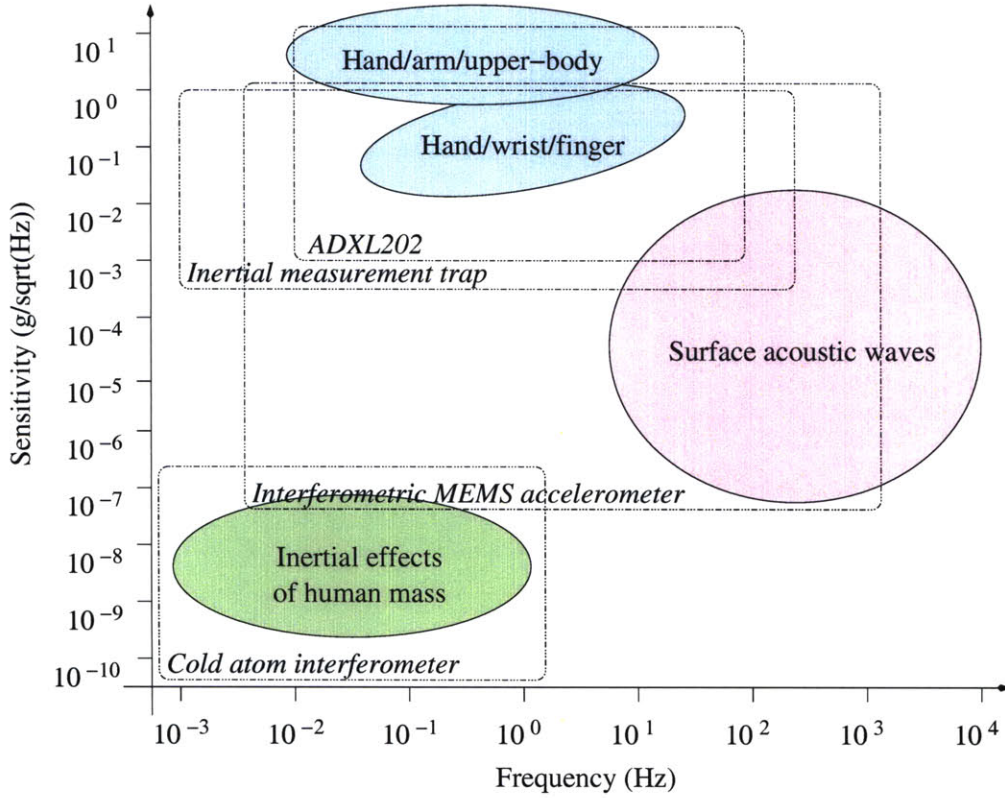


Figure 2.2. Inertial UI signals and sensor capabilities.

## 2.5 Generalized surface inertial channel

PINGPONGPLUS [17] determines the impact point of a ping-pong ball (or a finger tap) on a rigid surface by correlating the first arrival times of acoustic waves at multiple points on the surface, using electret microphones as detectors. The Responsive Window [25, 5] uses similar techniques to recover the location of finger and knuckle taps using piezoelectric film sensors bonded to the surface to detect surface acoustic waves.

As indicated in Figure 2.2, these signals are at the limit of sensitivity of the ADXL202. A more appropriate sensor for such signals would be the interferometric MEMS accelerometer [7]. A simple calculation based on the geometry shown in Figure 2.3 relates the angular resolution  $\phi$  of a two-point tap measurement to the distance  $\delta x$  between sensors  $a_1$  and  $a_2$ . The path length difference is  $\delta l = \delta x \sin \phi$ , hence

$$\phi = \sin^{-1} \frac{\delta l}{\delta x} \quad (2.7)$$

Letting  $c$  be the acoustic propagation velocity, a distance  $\delta l$  corresponds to a propagation delay

$$\delta t = \frac{\delta l}{c} \quad (2.8)$$

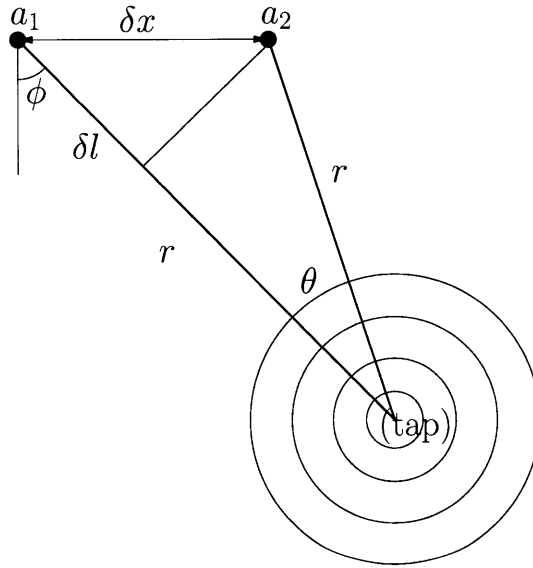
Given the system cutoff frequency  $f = 1/\delta t$ , the angular resolution works out to

$$\phi = \sin^{-1} \frac{c}{f \delta x} \quad (2.9)$$

For example, if the distance between accelerometers is  $\delta x = 15$  cm, the acoustic velocity is  $c = 450$  m/s (typical of safety glass), and the sampling frequency is  $f = 100$  kHz (typical of modern embedded microcontrollers), then the angular resolution works out to

$$\phi = \sin^{-1} \frac{(450 \text{ m} \cdot \text{s}^{-1})}{(100 \text{ kHz})(15 \text{ cm})} \simeq 1.72^\circ \quad (2.10)$$

which corresponds to a lateral position resolution of 2.5 cm at a distance of 1 meter.



**Figure 2.3.** Path difference  $\delta l$  of tap signal reaching two sensors  $a_1, a_2$  separated by distance  $\delta x$  ( $\phi \simeq \theta/2, r \gg \delta x$ ).

One immediate benefit to using an accelerometer with an appropriate surface mating is improved linearity in readout of the acoustic excitation. The microphonic pickup of PINGPONGPLUS and the PVDF sensor of the Responsive Window are both likely to have a nonlinear response to surface excitations, which complicates the process of inverting those signals to recover the epicenter of excitation (*i.e.* the tapping point.) It is worth noting that acoustic propagation in a shallow is highly dispersive

Another benefit is portability of the resulting sensor constellation. In PINGPONGPLUS and the Responsive Window, it was necessary to permanently affix sensors to the active surface in order to reduce noise and spurious signals.

Finally, the signal generated by the accelerometers permit inertial navigation as well as active surface sensing.

## 2.6 Inertial actuation

Inertial actuation is the inverse of inertial sensing, wherein a body in free space is able to arbitrarily accelerate or orient itself. This type of actuation is perhaps most familiar from vibrating pagers or mobile phones, which spin an unbalanced rotor to generate a cyclic inertial signal.

Artificial satellites also employ a form of inertial actuation to make fine orbital adjustment. By increasing or decreasing the rotation rate of internal rotors, a satellite can effect a torque on its rigid body, exploiting the principle of conservation of angular momentum.

Similarly, one might imagine a user interface that includes inertial actuation. A candidate actuator might be found in the miniature electrostatic gyroscope [23], in which a suspended spherical rotor provides an inertial reference for sensing rotations and accelerations. It is compelling to consider a single device that could provide both inertial sensing and actuation in a single package with a single sensing center.

## 2.7 A “hopping” actuator

A simple thought experiment suggests a more attainable actuator based on a multiplicity of unbalanced rotors and inertial feedback. Figure 2.4 illustrates the principle of locomotion of a rigid body with two internal unbalanced rotors and indicates the forces due to each rotor as well as their vector sum at the body center of mass.

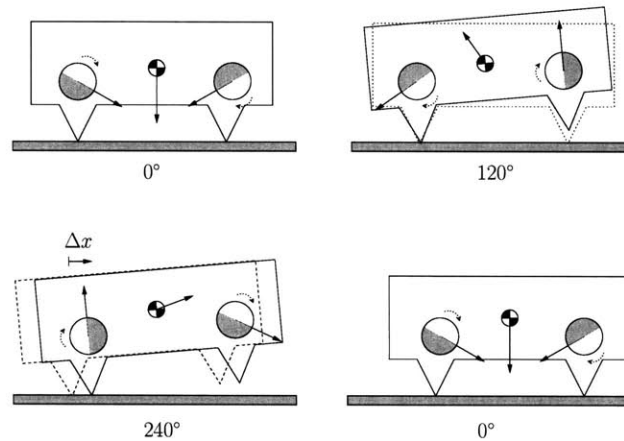
If the rotors spin with a fixed phase difference (here  $120^\circ$ ) they will exert a periodic force on the center of mass of the rigid body. Assuming a frictional contact between the rigid body and the supporting surface, the rotating force will on each cycle lift one end of the rigid body, push it forward, and then push it back down again. Reversing the phase difference between rotors will reverse the direction of locomotion.

## 2.8 A hopping kinetic display

When combined with inertial navigation to integrate paths of motion, the hopping actuation mode could be used to accurately position a hopping object. Furthermore, such an object could be entirely autonomous, with an embedded controller, battery or wireless power source, and wireless data link. To be capable of planar motion, an object needs only three points of support, each actuated by its own unbalanced rotor.

It is interesting to consider a multitude of coordinated, self-actuating autonomous objects acting as a kinetic display. While the details of the coordination scheme are beyond the present scope, it is worth pointing out the utility of the inertial channel for communication, ranging, and collision detection.

For example, hoppers might define separate communication channels by rotor spin frequency. A hopper's distance might be gauged by comparison of the signal amplitude received from each "foot-fall".



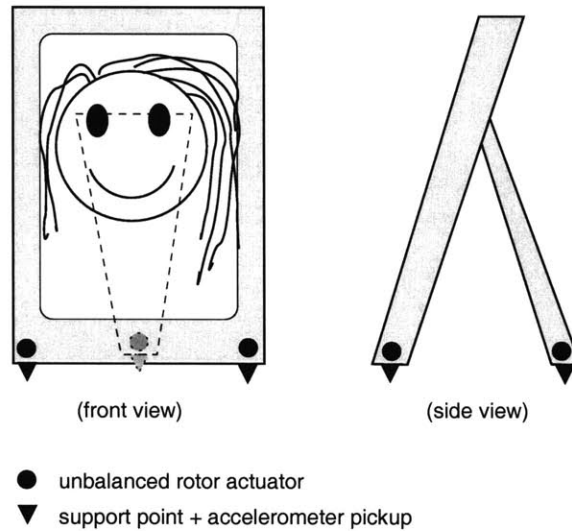
**Figure 2.4.** One "hop" cycle using unbalanced rotors dephased by  $120^\circ$ , resulting in a net displacement  $\Delta x$ .

## 2.9 The INERTIAL FRAME

The INERTIAL FRAME is a picture frame that provides an emotional frame of reference for inertial communication between users, and is intended to be an ambient, interpersonal haptic communicator.

In proposing this application for inertial sensing I have drawn on several prior works for inspiration, primarily: the LUMITOUCH emotional communication device [4], which lends the notion of a picture frame as the interface, adding new meaning to interactions with an object that is already familiar as the focus of emotional attention; the PINGPONGPLUS collaborative tangible interface [17], which points out the use of a surface as an interactive medium; and an as-yet unnamed sensor-augmented palm-sized PC [14], which exploits sensor fusion and behavioral modeling to enrich a portable computer's user interface.

The INERTIAL FRAME is sketched in Figure 2.5. It comprises a picture frame with an embedded controller and a constellation of accelerometers and actuators. A self-contained power source and wireless data link are assumed and not shown in this sketch.



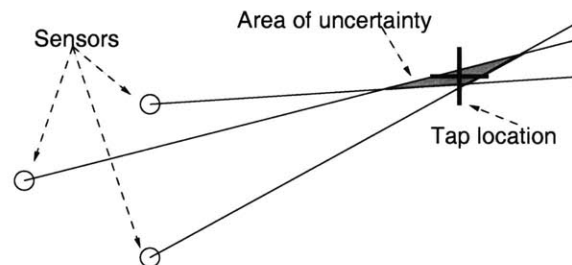
**Figure 2.5.** Schematic view of the Inertial Frame interpersonal haptic communication device.

The embedded controller generates three high-level channels from the raw inertial stream. First, low-frequency inertial data (e.g. below 100Hz) are integrated and conditioned by a Kalman filter to produce an inertial navigation channel that describes the motion of the entire system, permitting the use of the INERTIAL FRAME as a gestural sensor.

Secondly, the inertial data are Fourier-transformed and fed to a behavioral model (as in [14]) that recognizes patterns of user behavior transmitted through the supporting surface, such as impatient finger-drumming, typing, writing, etc. Intentional gestures such as finger or stylus taps may also be detected through this channel.

Finally, pairwise differences of inertial signals will reveal propagating surface excitations. These difference signals may then be time-correlated to obtain the direction of propagation (as in [25, 5]). Three receivers yield three pairwise differences and hence three signal source orientations.

These channels may of course be used in combination. For example, the behavioral channel can be used to recognize stylus taps and the orientation channel may be used to recover tap points.



**Figure 2.6.** Tap location using multiple orientations.

The three propagation directions obtained above also permit location of the signal source on the surface: two oriented lines intersect at a unique point (or not at all) and the intersection points of three oriented lines will form a triangle around the signal source (see Figure 2.6).

Finally, the raw inertial signals may be filtered and replayed by the receiving INERTIAL FRAME using the unbalanced rotors described above either to effect motion of the entire object or simply to create tangible disturbances (audible or vibratory) on the tabletop.

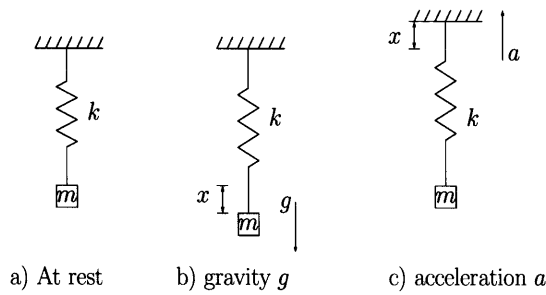
It is worth noting that, of the inertial channels derived from sensor data by the INERTIAL FRAME, all but the orientation channel may be reasonably obtained from existing sensors. This suggests that the INERTIAL FRAME might be built today and later enhanced by the addition of accelerometers with the wider bandwidth and greater sensitivity necessary to provide a high-resolution orientation channel.



# Chapter 3

## Inertial effects in particle traps

Most accelerometers trace their origins to the simple harmonic oscillator, comprising a known (“proof”) mass  $m$  and a spring with a known tension/extension ratio  $k$ . In Figure 3.1a, this system is shown at equilibrium. When a gravitational field is imposed as in Figure 3.1b, the upward force exerted by the spring balances the downward force due to gravity, that is,  $F_{\text{spring}} = kx = mg = F_{\text{gravity}}$ , permitting derivation of the applied acceleration  $g = kx/m$  from known quantities. A similar situation is depicted in Figure 3.1c, but in this case the force exists between the mass (as it tends to remain at rest) and its constraining frame of reference.



**Figure 3.1.** Spring-mass accelerometer.

It is worth noting that this is the basic operational principle of nearly all classical accelerometers. Accelerometer design is a combination of efforts to increase sensitivity to inertial signals, to decrease total system noise, and to broaden response about the resonant frequency

$$\omega_0 = \sqrt{\frac{k}{m}}. \quad (3.1)$$

We will return to this model later in the chapter to explore the role of noise in accelerometry. First we consider the mechanics of proof mass suspension in particle traps.

### 3.1 The particle trap as accelerometer

The following discussion will consider only electrodynamic particle traps, of which the Paul trap [26] is a well-known example. A particle is said to be trapped if it is elastically bound to an axis or coordinate in space by a restoring force. For simplicity’s sake we will consider a particle bound by a linear restoring force  $F = -\vec{k} \cdot \vec{r}$ , implying a quadratic potential

$$W \propto (ax^2 + \beta y^2 + \gamma z^2) \quad (3.2)$$

surrounding the constraint coordinate. As the system evolves classically to minimize its potential energy, the particle's motion will describe an orbit centered about the minimum of this parabolic potential. Such a potential is preferred because it is one of only two potentials that leads to harmonic motion – the other being an inverse-law ( $r^{-1}$ ) potential.

If it were possible to construct a parabolic potential minimum in free space, a three-dimensional accelerometer could be constructed trivially by suspending a charged particle in a static field and reading out its position by electrometry, optical interferometry, or other means. It is therefore unfortunate that Earnshaw's theorem pertains: maxima (or minima) of the electric potential cannot be imposed at points in free space. This follows from the divergence of the electric field in free space

$$\nabla \cdot \vec{E} = 0 \quad (3.3)$$

and the relation between the electric field and the electric potential

$$\vec{E} = -\nabla \Phi \quad (3.4)$$

which yield the Laplace equation

$$\nabla^2 \Phi = (\partial_x^2 + \partial_y^2 + \partial_z^2) \Phi = 0. \quad (3.5)$$

Note that this equation admits no static convex solutions. Now consider a saddle-shaped potential such as  $z = x^2 - y^2$ . Such a potential forms the basis of the Paul trap [26] by creating a hyperbolic fixed point in the trap's dynamics.

The Paul trap potential assumes a parabolic potential geometry and a harmonic time dependence

$$\Phi(\vec{r}, t) = \frac{\Phi_0}{a_0^2} (\alpha x^2 + \beta y^2 + \gamma z^2) \quad (3.6)$$

where  $a_0$  is the absolute scale of the trap, determined by its three characteristic radii

$$a_0^2 = |\alpha| x_0^2 + |\beta| y_0^2 + |\gamma| z_0^2 \quad (3.7)$$

and  $\Phi_0$  is the time-dependent potential

$$\Phi_0 = U + V \cos \omega_0 t \quad (3.8)$$

The Laplace equation requires  $\nabla^2 \Phi = 0$  everywhere in the free volume of the trap, so the above potential yields

$$\nabla^2 \Phi = \frac{\Phi_0}{a_0^2} 2(\alpha + \beta + \gamma) \quad (3.9)$$

Two points are immediately apparent. First, the scale of effects in the trap will be determined by  $\Phi_0/r_0^2$ . Second, the field geometry will have a constraint

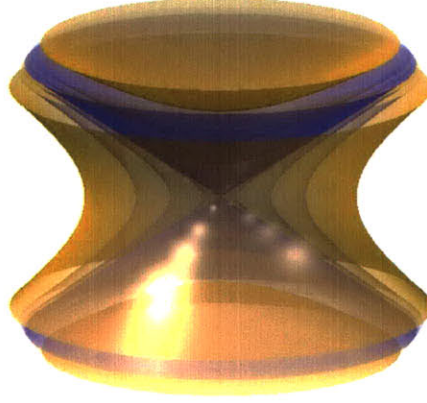
$$\alpha + \beta + \gamma = 0 \quad (3.10)$$

to be satisfied.

The values  $\alpha = \beta = 1$  and  $\gamma = -2$  provide a simple solution to this constraint and yield the geometry of the familiar three-dimensional Paul trap. By writing the radius as  $r^2 = x^2 + y^2$  we obtain

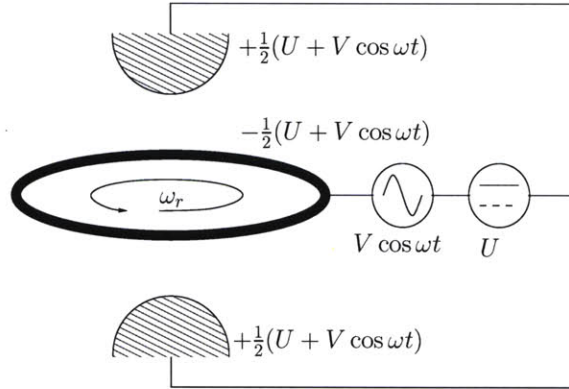
$$\Phi(\vec{r}, t) = \Phi_0(r^2 - 2z^2) \quad (3.11)$$

which has the hyperbolic form illustrated in Figure 3.2.



**Figure 3.2.** Isopotential surfaces of  $\Phi \propto (r^2 - 2z^2)$ .

Because hyperbolic shells are difficult both to draw and to fabricate, a Paul trap is often depicted schematically as in Figure 3.3.



**Figure 3.3.** 3D Paul trap (schematic).

The potential difference between the ring electrode and the end caps is  $\Phi_0$  and the corresponding force acting on the particle is

$$\vec{F}(\vec{r}, t) = -e \nabla \Phi(\vec{r}, t). \quad (3.12)$$

Writing out the Hamiltonian for this system, we add a potential energy term to account for accelerational shifts  $\vec{s}(t)$  of the trapping frame:

$$\mathcal{H} = T + V = \frac{p^2}{2m} + \Phi(\vec{x}, t) q + m(\vec{s}(t) \cdot \vec{x}) \quad (3.13)$$

From this Hamiltonian we obtain the system's equations of evolution

$$\begin{aligned}\dot{\vec{x}} &= \partial_{\vec{p}} \mathcal{H} = \frac{1}{m} \vec{p} \\ \dot{\vec{p}} &= -\partial_{\vec{x}} \mathcal{H} = -m \vec{s} - \frac{\Phi_0 e}{a_0^2} \begin{bmatrix} 2x \\ 2y \\ -4z \end{bmatrix}\end{aligned}\quad (3.14)$$

which may be restated as the driven equations of motion

$$\begin{bmatrix} \ddot{x} \\ \ddot{y} \\ \ddot{z} \end{bmatrix} + \frac{\Phi_0 e}{m a_0^2} \begin{bmatrix} 2x \\ 2y \\ -4z \end{bmatrix} = \begin{bmatrix} s_x \\ s_y \\ s_z \end{bmatrix}\quad (3.15)$$

Because these three decoupled equations are similar up to a constant we will consider only the first,

$$\ddot{x} + \frac{e}{m a_0^2} (U + V \cos \omega_0 t) 2x = 0\quad (3.16)$$

which recalls the Mathieu equation

$$\ddot{x} + (a + 2q \cos 2\tau)x = 0\quad (3.17)$$

whose stability depends on the dimensionless parameters  $a$  and  $q$ .

By comparing the Mathieu equation (3.17) with the ion trap equation of motion (3.16), we can identify the parameterization

$$a = \frac{-16eV}{m\omega_0^2 a_0^2}, \quad q = \frac{8eU}{m\omega_0^2 a_0^2}, \quad \tau = \frac{\omega_0}{2} t\quad (3.18)$$

necessary to determine operational stability.

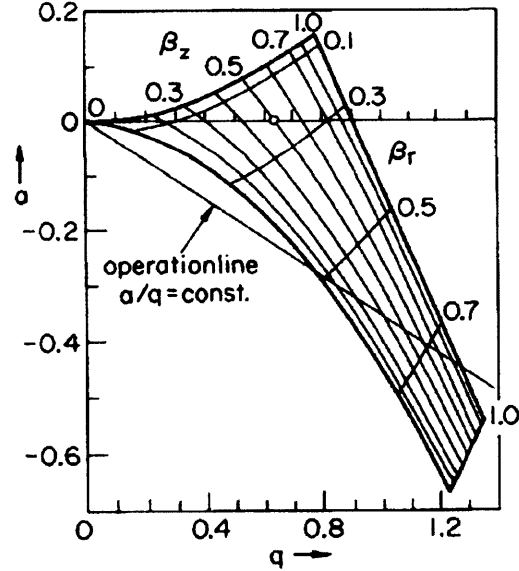


Figure 3.4. Lowest stability region in ion trap (revised from [26]).

Figure 3.4 illustrates the lowest trapping region of the three-dimensional Paul trap. Note the parameters  $\beta_r$  and  $\beta_z$  which relate a trapped particle's fast *micromotion* of frequency  $\omega_0$  to its *secular* motion in the  $r$  plane and the  $z$  axis by

$$\omega_r = \beta_r \omega_0, \quad \omega_z = \beta_z \omega_0. \quad (3.19)$$

## 3.2 Derivation of the pseudopotential

Consider the static and oscillating components of the force acting on a trapped particle

$$F(\vec{x}, t) = f_s(\vec{x}) + f_o(\vec{x}, t) \quad (3.20)$$

where

$$f_s = -e \partial_x \varphi_{\text{static}}(\vec{x}) = -e U \partial_x \phi_g \quad (3.21)$$

$$f_o = -e V (\cos \omega_0 t) \partial_x \phi_g = f \cos \omega_0 t \quad (3.22)$$

and

$$f = -e V \partial_x \phi_g \quad (3.23)$$

$$\phi_g = \frac{\alpha x^2 + \beta y^2 + \gamma z_0^2}{a_0^2} \quad (3.24)$$

Now assume the following: the secular motion  $S(t)$  and the micromotion  $M(S, t)$  are known, that  $S \gg M$  (the secular motion is much greater than the micromotion), and that  $\dot{S} \ll \dot{M}$  (the secular motion is much slower than the micromotion). Rewrite the total motion as

$$X(t) = S(t) + M(S, t) \quad (3.25)$$

noting that  $M$  depends on and is considered to be a perturbation of  $S$ .

Now that the motion has been separated into components with two distinct characteristic time scales, it becomes amenable to *two-timing* analysis [30]. Micromotion occurs on a fast time scale

$$\tau = \frac{2\pi}{\omega_0} \quad (3.26)$$

compared to the secular motion and averages to zero in a single period:

$$\langle M(t) \rangle_\tau = \int_0^\tau M(t) dt \simeq 0. \quad (3.27)$$

Expanding the equation of motion in  $M$  around a path described by  $S$

$$m \ddot{x} = F(\vec{x}, t) = m(\ddot{S} + \ddot{M}) = f_s(S) + f_o(S, t) + \left[ \sum_{k=1}^N \frac{M^k}{k!} \partial_x^k \right] (f_s(x) + f_o(x, t)) \Big|_{x=S} \quad (3.28)$$

to first order yields

$$m(\ddot{S} + \ddot{M}) = f_s(S) + f_o(S, t) + M (\partial_x f_s(x) \Big|_{x=S} + \partial_x f_o(x, t) \Big|_{x=S}) \quad (3.29)$$

By supposing that  $m\ddot{M} \simeq f_o(S, t)$ , an approximate solution for  $M(S, t)$  can be found by integration:

$$M(S, t) \simeq -\frac{1}{m\omega_0^2} f(S) \cos \omega_0 t \quad (3.30)$$

In this approximation, the micromotion  $M$  is found to be harmonic with frequency  $\omega$ , phase opposite to the driving signal, amplitude depending on the secular motion, and average kinetic energy

$$\langle k_M \rangle = \frac{f^2(S)}{4m\omega_0^2} \quad (3.31)$$

Equations for slow secular motion  $S(t)$  can be found by averaging  $m(\ddot{S} + \ddot{M})$  over one period  $\tau$  of micromotion and using the approximate solution (3.30) for  $M(S, t)$ :

$$\langle m(\ddot{S} + \ddot{M}) \rangle = \langle f_s(S) \rangle + \langle f_o(S, t) \rangle + \left\langle M \frac{\partial f_s(x)}{\partial x} \Big|_{x=S} \right\rangle + \left\langle M \frac{\partial f_o(x, t)}{\partial x} \Big|_{x=S} \right\rangle \quad (3.32)$$

Only the  $\ddot{S}$ ,  $f_s$ , and  $\cos^2$  terms survive averaging:

$$\langle m(\ddot{S} + \ddot{M}) \rangle = \langle f_s(S) \rangle + \left\langle M \frac{\partial f_o(x, t)}{\partial x} \Big|_{x=S} \right\rangle \quad (3.33)$$

$$\frac{1}{\tau} m \int_0^\tau \ddot{S} dt = \frac{1}{\tau} \int_0^\tau f_s(S) dt - \frac{1}{m\omega_0^2} \frac{1}{\tau} \int_0^\tau f(x) \cos \omega_0 t \partial_x f_o(x) \cos \omega_0 t \Big|_{x=S} dt \quad (3.34)$$

leaving

$$m \ddot{S} = f_s(S) - \frac{1}{2m\omega_0^2} [f(x) \partial_x f(x)]_{x=S} \quad (3.35)$$

By expressing  $f_s$  and  $f$  as derivatives of the pseudo- and secular potentials  $\varphi_{ps}$  and  $\varphi_{sec}$  we obtain the definition of  $\varphi_{sec}$

$$m \ddot{S} = -\partial_x (eU\phi_g(x) + \varphi_{ps}(x)) \Big|_{x=S} \equiv -\partial_x \varphi_{sec}(x) \Big|_{x=S} \quad (3.36)$$

where

$$\varphi_{ps}(x) \equiv \frac{e^2}{4m\omega_0^2} (V(\cos \omega_0 t) \partial_x \phi_g)^2 \quad (3.37)$$

The average of the pseudopotential over one cycle is of most interest in understanding the comparatively slow secular motion:

$$\begin{aligned}
\langle \varphi_{\text{ps}} \rangle &= \frac{1}{\tau} \int_0^\tau \varphi_{\text{ps}}(t) dt \\
&= \frac{e^2 V^2}{4m\omega_0^2} (\partial_x \phi_g(x))^2 \frac{1}{\tau} \int_0^\tau \cos^2 \omega_0 t dt \\
&= \frac{e^2 V^2}{2m\omega_0^2} \left( \frac{x}{x_0^2 + y_0^2 + 2z_0^2} \right)^2
\end{aligned} \tag{3.38}$$

From the last form it is clear that the pseudopotential is approximately quadratic for the given conditions  $S \gg M$  and  $\ddot{S} \gg \ddot{M}$ .

### 3.3 Inertial signature in trap dynamics

A clear inertial signature appears in the approximate system described by the pseudopotential (3.38). To see this, start by assuming that a trapped particle oscillates harmonically to first order as it moves in the quadratic pseudopotential  $\varphi_{\text{ps}}$ . This oscillation has a secular frequency  $w_s = \beta_s \omega$  ( $0 \leq \beta_s \leq 1$ ), distinct from the particle's micromotion at the trap frequency  $\omega$ .

Let the Hamiltonian for a particle trapped in a pseudopotential and subject to an acceleration  $s$  be

$$H = \frac{p^2}{2m} + \varphi_{\text{ps}}(x) + m s x = \frac{1}{2m} (p^2 + \kappa x^2) + m s x \quad \text{where } \kappa = \left( \frac{eV}{\omega_0 a_0^2} \right)^2 \tag{3.39}$$

The equation of motion will be that of the driven harmonic oscillator

$$\ddot{x} + \omega_s^2 x = -s \tag{3.40}$$

where  $\omega_s^2 = \kappa/m$ . By substituting the general solution  $x = \bar{x} + c_0 e^{i\omega_s t} + c_1 e^{-i\omega_s t}$  into this equation, one quickly finds that the particle oscillates about a mean position

$$\bar{x} = \langle x \rangle = -\frac{1}{\omega_s^2} s = -\frac{m^2 \omega_s^2 a_0^4}{e^2 V^2} s. \tag{3.41}$$

This mean position is equivalent to the secular position  $S(t)$  identified above. Recalling that the micromotion  $M$  depends on  $S \approx \bar{x}$ , the RMS amplitude of  $M(\bar{x}, t)$  is found to be

$$\sqrt{\langle M(\bar{x}, t)^2 \rangle} = \left[ \frac{1}{\tau} \int_0^\tau \left( \frac{eV}{m\omega_0^2} \right)^2 \cos^2 \omega_0 t \left( \frac{2\bar{x}}{a_0^2} \right)^2 dt \right]^{\frac{1}{2}} = \sqrt{2} \frac{eV}{m\omega_0^2} \frac{\bar{x}}{a_0^2} \tag{3.42}$$

Finally, by substituting the mean value  $\bar{x}$  from above into the RMS amplitude

$$M^{rms} = \sqrt{\langle M(\bar{x}, t)^2 \rangle} = \frac{eV}{m\omega_0^2} \frac{\sqrt{2}}{a_0^2} \bar{x} = -\frac{\omega_s^2}{\omega^2} \frac{m a_0^2 \sqrt{2}}{eV} s \quad (3.43)$$

one finds that  $\bar{x}$  and  $M^{rms}$  both depend linearly on the applied acceleration  $s$ . We have learned that a trapped particle has two constants of motion directly proportional to applied accelerations, and that these constants of motion are decoupled for all three degrees of freedom.

### 3.4 Geometry of a 3-symmetric inertial measurement trap

The Paul trap as described above has a preferred axis and a corresponding radial symmetry, adequate for applications in which particles are kept close to the equilibrium position. In developing an inertial measurement unit, however, it is preferable to have equivalent equations of motion in all three directions. What follows is a derivation of the electrode geometry for such a trap.

To obtain closed forms for the potential, we wish to satisfy both

$$\nabla^2 \phi = 0 \quad (3.44)$$

and

$$\phi = \alpha x^2 + \beta y^2 + \gamma z^2 \quad (3.45)$$

Equation (3.44) leads to the condition

$$\alpha + \beta + \gamma = 0 \quad (3.46)$$

Two common choices of geometric factors which satisfy this condition are

$$\alpha = 1, \beta = -1, \gamma = 0 \quad (3.47)$$

for the linear quadrupole trap,

$$\alpha = 1, \beta = 1, \gamma = -2 \quad (3.48)$$

for the three-dimensional quadrupole trap, and the general form

$$\alpha = A\beta, \gamma = -(A+1)\beta \quad (3.49)$$

where  $A = 1$  corresponds to the circular quadrupole trap and  $A > 1$  corresponds to the elongated, elliptical quadrupole trap. These are the most commonly considered solutions and practical approximations are often made to reduce fabrication complexity [3] or to enhance certain trapping configurations in many-body systems [11].



In Paul's two-phase systems, the electrode geometry is defined by isosurfaces of (3.45) corresponding to the phase factors 1 and -1. This can be generalized to multi-phase systems with isosurfaces defined by the modulus of  $\phi$  and partitioned by the phase of  $\phi$ . For example, the complex geometric factors

$$\alpha = 1, \beta = e^{i\pi\frac{2}{3}}, \gamma = e^{i\pi\frac{4}{3}} \quad (3.50)$$

(*i.e.*, complex cube roots of unity) will satisfy condition (3.46). The isosurfaces of this form are determined by solving  $|\phi| = a$  or equivalently  $|\phi|^2 = a^2 = \phi^* \phi = (\text{Re } \phi)^2 + (\text{Im } \phi)^2$ , which yields the polytope

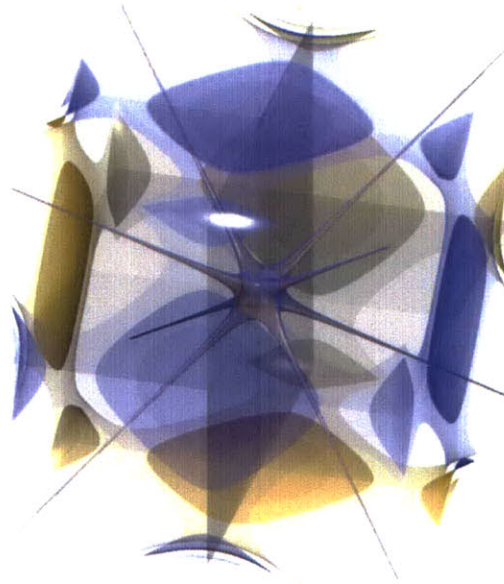
$$x^4 + y^4 + z^4 - x^2y^2 - y^2z^2 - z^2x^2 = a^2 \quad (3.51)$$

or equivalently

$$a^2 = \frac{1}{2} [(x^4 - 2x^2y^2 + y^4) + (y^4 - 2y^2z^2 + z^4) + (z^4 - 2z^2x^2 + x^4)] \quad (3.52)$$

$$(x^2 - y^2)^2 + (y^2 - z^2)^2 + (z^2 - x^2)^2 = 2a^2 \quad (3.53)$$

as shown in Figure 3.5.

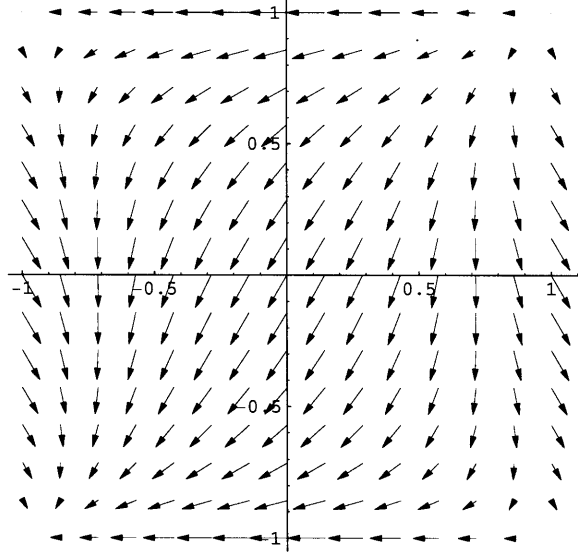


**Figure 3.5.** Isosurfaces of  $|\alpha x^2 + \beta y^2 + \gamma z^2| = \{1, 9.4\}$ .

As before, the Laplace equation  $\nabla^2 \phi = 0$  leads to the constraint  $\alpha + \beta + \gamma = 0$ , which is satisfied by this choice of phase factors  $\alpha, \beta, \gamma$ . Furthermore,  $\text{Re}(\alpha + \beta + \gamma) = 0$  is a hint that these phase factors will be relevant to the dynamics of a real harmonic system.

Finally we must confirm that the isopotential surface, which naturally partitions into fcc (face-centered, cubic) regions, is likewise partitioned in phase so that each region has a single phase. By symmetry, we need only demonstrate this for one face (*i.e.*,  $z=1$ ) and only on one quadrant of that face.

Because the phase of  $\phi$  is determined by the factors  $\alpha, \beta, \gamma$ , it is independent of radius and the phase can be fully characterized by mapping it on the region  $\{x=[0, 1], y=[0, 1], z=1\}$ . Figure 3.6 reveals that the phase on this face varies over the interval  $[-\pi, -\frac{\pi}{3}]$  (which can be readily proven), therefore the faces of the cube are each partitioned in phase to one-third of the unit circle.



**Figure 3.6.** Phase plot of  $\alpha x^2 + \beta y^2 + \gamma z^2|_{z=1}$ .

Starting once again with the full form of the electric potential

$$\Phi(\vec{r}, t) = \frac{\Phi_0}{r_0^2} (\alpha x^2 + \beta y^2 + \gamma z^2) \quad (3.54)$$

and the force arising from it

$$\vec{F}(\vec{r}, t) = -e \nabla \Phi(\vec{r}, t) \quad (3.55)$$

we can write the system Hamiltonian

$$\mathcal{H} = T + V = \frac{p^2}{2m} + \Phi(\vec{x}, t) e + m(\vec{s}(t) \cdot \vec{x}) \quad (3.56)$$

and obtain the system's equations of evolution (adding a viscous drag term where  $r$  is the radius of the particle in question,  $\eta$  is the viscosity of the medium through which it moves, and  $\vec{c} = [\alpha, \beta, \gamma]^T$ )

$$\begin{aligned} \dot{\vec{x}} &= \partial_{\vec{p}} \mathcal{H} = \frac{1}{m} \vec{p} \\ \dot{\vec{p}} &= -\partial_{\vec{x}} \mathcal{H} = -\frac{2\Phi_0 e}{r_0^2} (\vec{c} \cdot \vec{x}) - 6\pi r \eta \dot{\vec{x}} - m \vec{s} \end{aligned} \quad (3.57)$$

leading to the driven, dissipative equations of harmonic motion

$$\ddot{\vec{x}} + \frac{6\pi r\eta}{m} \dot{\vec{x}} + \frac{2\Phi_0 e}{r_0^2} \vec{c} \cdot \vec{x} = \vec{s} \quad (3.58)$$

### 3.5 Accelerometer noise models

Error in measured acceleration may be attributed chiefly to 1) noise *inherent* to proof mass motion and 2) noise in the *readout* of proof mass motion. We will return to the issue of readout error in the sections on experimental methods and results, and for now consider only the inherent motional noise.

Of the mechanisms contributing to motional noise of trapped (macroscopic) particles, we consider the leading sources to be phase/magnitude error in the trapping field and thermomechanical effect. Since the effective spring constant depends quadratically on the trapping voltage, which is readily determined to 1 part in  $10^4$ , errors due to trapping field amplitude are taken to be small.

Phase errors in the field are taken to be uncertainties in trapping frequency, upon which the effective spring constant again depends quadratically; if they are considered as fractions of cycles, their noise contribution is seen to be smaller still than errors in field magnitude. More importantly, these effects are more amenable to control than thermal effects.

To estimate thermal noise effects in a particle's motion, we invoke the theorem of energy equipartition among quadratic degrees of freedom. The equipartition theorem applies both because the pseudopotential is quadratic and because we can reasonably assume that micron-scale particles in air at room temperature are in thermal equilibrium with their environment.

The expected free energy in a thermal degree of freedom is  $k_B T/2$  and variations in the pseudopotential will go as

$$\langle \delta\varphi_{\text{ps}} \rangle = \frac{\kappa}{2} \langle (\delta x)^2 \rangle \quad (3.59)$$

so the motional noise will be on the scale of

$$\delta x = \sqrt{\frac{k_B T}{\kappa}} \quad (3.60)$$

Because readout of acceleration is taken to be  $a = -\kappa x/m$ , the scale of thermal noise effects in acceleration measurements will be

$$|\langle \delta a \rangle| = \frac{\kappa}{m} \langle \delta x \rangle = \sqrt{\frac{\kappa k_B T}{m^2}} = \frac{eV}{m\omega_0 a_0^2} \sqrt{\frac{k_B T}{m}} \quad (3.61)$$

If the accelerometer is operating in a dissipative regime, it can be thought of as a damped resonator and described by the equation of motion

$$m \ddot{x} + \nu \dot{x} + \kappa x = 0 \quad (3.62)$$

and solutions derived by substitution of  $x = e^{\lambda t}$  to obtain the characteristic equation

$$(m\lambda^2 + \nu\lambda + \kappa) = 0 \quad (3.63)$$

with solutions

$$\lambda_{1,2} = \frac{-\nu \pm \sqrt{\nu^2 - 4m\kappa}}{2m} = \frac{\nu^2}{2m} \left( -1 \pm \sqrt{1 - \left(\frac{2m\omega}{\nu}\right)^2} \right) \quad (3.64)$$

There are four regimes of solutions, depending on the eigenvalues  $\lambda_{1,2}$ :

<b>Re(<math>\lambda_{1,2}</math>)</b>	<b>Im(<math>\lambda_{1,2}</math>)</b>	<b>Classification</b>	
= 0	$\neq 0$	undamped	
$\neq 0$	$\neq 0$	damped	(3.65)
= 0	= 0	critically damped	
$\neq 0$	= 0	overdamped	

The system quality factor is a measure of energy loss per cycle or spectral width of a resonance,

$$Q = \left\langle \frac{-U}{\Delta U} \right\rangle_{\text{cycle}} = \frac{\omega_0}{\Delta\omega} = [\text{Re}(\lambda)]^{-\frac{2\pi}{\omega}} \quad (3.66)$$

For the damped resonator,

$$Q = \frac{m\omega_0}{\nu} = \frac{\sqrt{m\kappa}}{\nu} \quad (3.67)$$

and the transfer function in terms of Q can be expressed

$$|G(f)|^2 = \frac{1}{(1-f^2)^2 + \frac{f^2}{Q^2}} \quad \left( f = \frac{\omega}{\omega_0} \right) \quad (3.68)$$

The thermal energy in a damped resonator will be distributed over its entire spectrum

$$\frac{1}{2} k_B T = \int_0^\infty G\left(\frac{\omega}{\omega_0}\right) \langle E(\omega) \rangle d\omega \quad (3.69)$$

Taking  $G(f)$  to be normalized the thermal motional noise density will be

$$\langle (\delta x)^2 \rangle = \frac{4k_B T}{\kappa} \left| G\left(\frac{\omega}{\omega_0}\right) \right|^2 \quad (3.70)$$

and finally, the noise density in acceleration readout due to these effects will be

$$\begin{aligned} |\delta a| &= \frac{\kappa}{m} \sqrt{\langle (\delta x)^2 \rangle} \\ &= \sqrt{\frac{4\kappa k_B T}{m^2}} \left| G\left(\frac{\omega}{\omega_0}\right) \right| \\ &= \frac{eV}{m\omega_0 a_0^2} \sqrt{\frac{k_B T}{m}} \left| G\left(\frac{\omega}{\omega_0}\right) \right| \end{aligned} \quad (3.71)$$

Now we turn to experimental methods to demonstrate these effects.

# Chapter 4

## Experimental methods

We have shown that the motion of a particle in a Paul trap has two (leading) characteristic timescales corresponding to a slow secular motion  $S(t)$  and a fast micromotion  $M(S, t)$ . These in turn depend linearly on an inertial term in the trap's governing equation. This inertial signature is expected to be a robust effect in traps with quadratic confining potentials. Here, we demonstrate these effects in both numerical and physical experiments.

### 4.1 Simulation of an inertial measurement trap

To observe the previously derived inertial terms in simulation, we start with the term  $(-\nu\vec{p})$  to model dissipation:

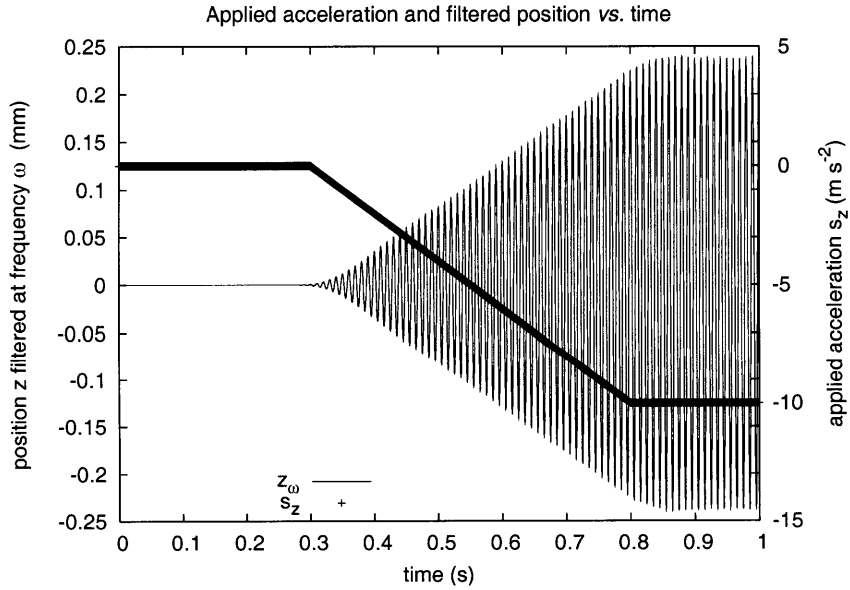
$$\begin{aligned}\dot{\vec{x}} &= \partial_{\vec{p}}\mathcal{H} = \frac{1}{m}\vec{p} \\ \dot{\vec{p}} &= -\partial_{\vec{x}}\mathcal{H} = m\vec{s} - \nu\vec{p} - \frac{\Phi_0 e}{a_o^2} \begin{bmatrix} 2x \\ 2y \\ -4z \end{bmatrix}\end{aligned}\tag{4.1}$$

This set of six linear, coupled differential equations are then numerically integrated to obtain the motion  $\vec{x}(t)$  using a fourth-order fixed-step Runge-Kutta algorithm[27].

Parameters were chosen to simulate the operation of a macroscopic oil droplet trap [28] and a time-dependent acceleration  $s_z$  was applied to accelerate the trap upward. The relevant parameters are

$$\begin{aligned}
 x_0, y_0 &= 2.5 \text{ mm} \\
 z_0 &= 5.0 \text{ mm} \\
 U &= 0 \text{ V} \\
 V &= 1.0 \text{ kV} \\
 \omega &= 2\pi \cdot 100 \text{ Hz} \\
 r_{\text{particle}} &\simeq 10 \mu\text{m} \\
 m_{\text{particle}} &= 9.3 \mu\text{g} \\
 e_{\text{particle}} &= 1.3 \text{ mC} \cdot \text{g}^{-1}
 \end{aligned} \tag{4.2}$$

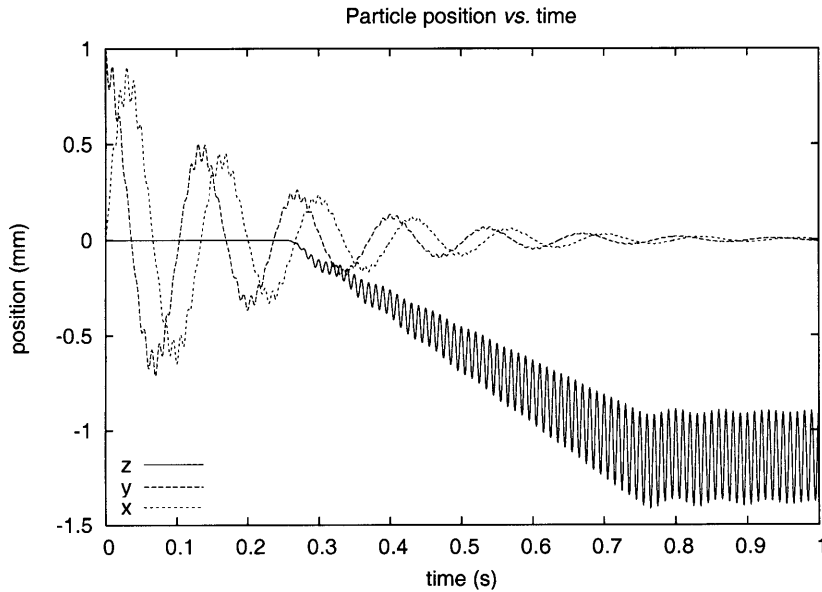
while the simple dissipation term has a prefactor  $\nu = 10$ , chosen to provide an underdamped simulation.



**Figure 4.1.** Particle micromotion compared with applied acceleration (simulated).

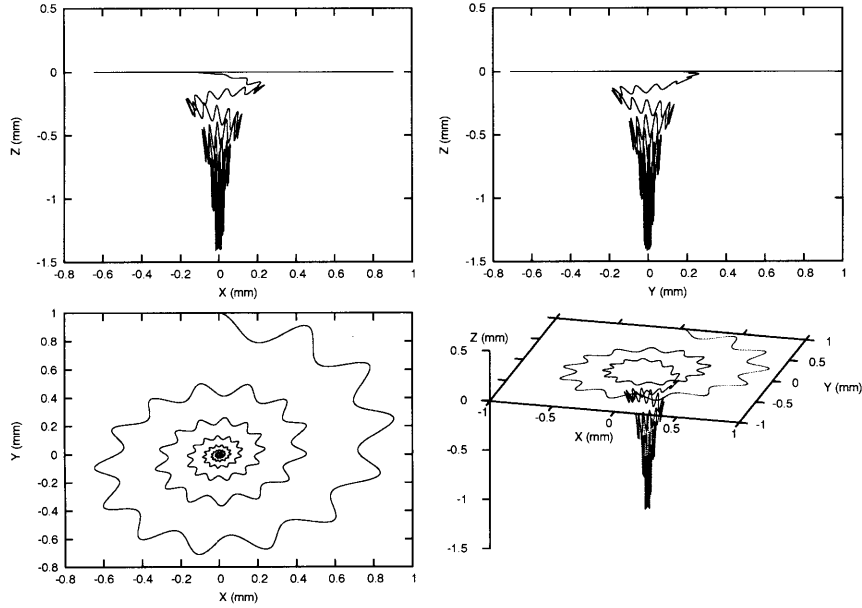
Figure 4.1 compares the micromotion  $z_\omega$  of a trapped particle with the applied acceleration as  $s_z$  goes from 0 to  $-10 \text{ m} \cdot \text{s}^{-2}$ , illustrating the linear relationship between the two. In this case  $z_\omega$  represents the particle position  $z$  filtered in a narrow band around the excitation frequency  $\omega$  by a third-order Chebyshev FIR filter. This filtering leads to the time-delayed response seen in the graph.

The linear relationship of micromotion on acceleration is also apparent in the graphs of position *vs.* time shown in Figure 4.2 for each of the particle's Cartesian coordinates. The particle's orbit starts out from the injection point  $(x, y, z) = (0, 1, 0)$  and is seen to decay due to damping. As the particle moves farther from equilibrium on any axis, its micromotion along that axis increases. From  $t = 0.25$  to  $0.75$  s, the applied acceleration  $s_z$  is ramped down, causing variations in micromotion amplitude  $M_z^{rms}$  and mean position  $\bar{z}$ .



**Figure 4.2.** Simulated particle trajectory in trap in each axis.

Finally, Figure 4.3 shows the particle's trajectory projected onto the three principle planes and in a rotated orthogonal projection. The orbit in the  $xy$  plane is seen to decay toward equilibrium, even as the equilibrium point moves downward and the micromotion in  $z$  increases.



**Figure 4.3.** Projections of simulated particle trajectory.

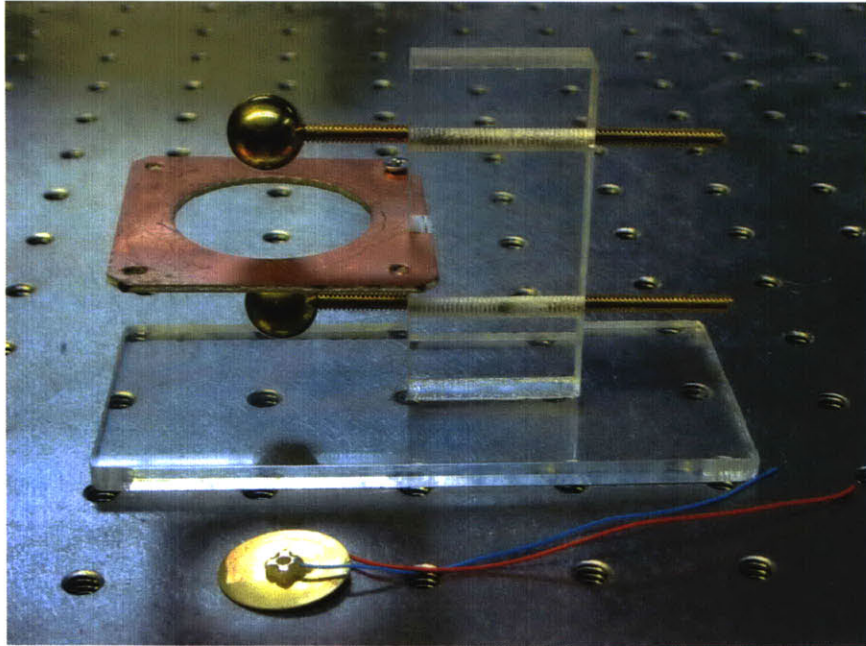
This simulation is representative of several numerical experiments run with parameters corresponding to stable trapping and suggests that it is reasonable to seek similar results in physical experiments.

## 4.2 Physical realization of Paul traps

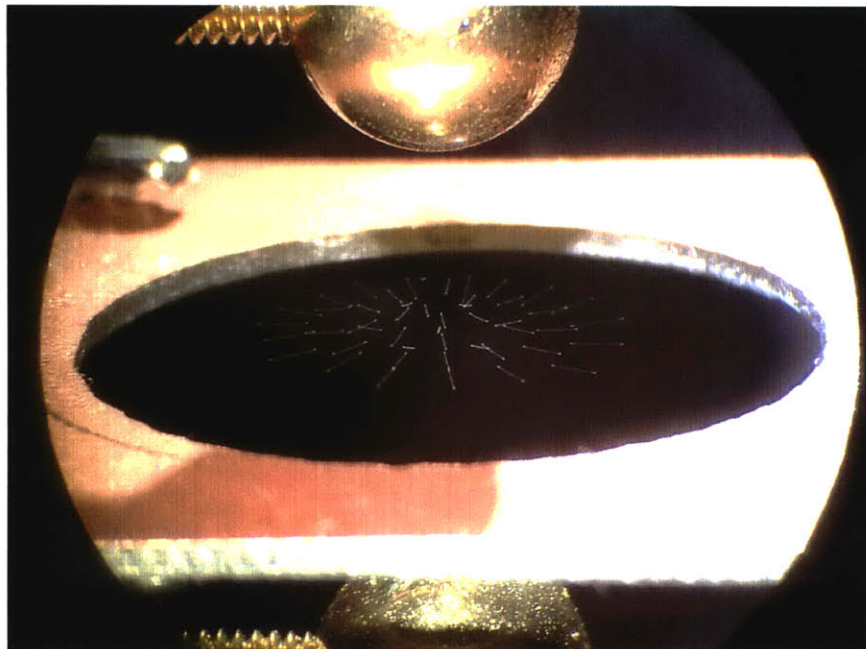
The classic Paul trap is an exquisite assembly of precision-machined hyperboloid shells. In practice, however, almost any quadrupolar arrangement of electrodes will yield a workable trap. A common configuration of electrodes such as might be used in a classroom demonstration [28] is shown in the background of Figure 4.4, and was used to create the images in Figures 4.5 and 4.6. In contrast,



the simplified planar trap used in IMIT 1.0 is shown in the foreground of Figure 4.4.



**Figure 4.4.** Demonstration trap (background) and simplified planar trap (foreground).

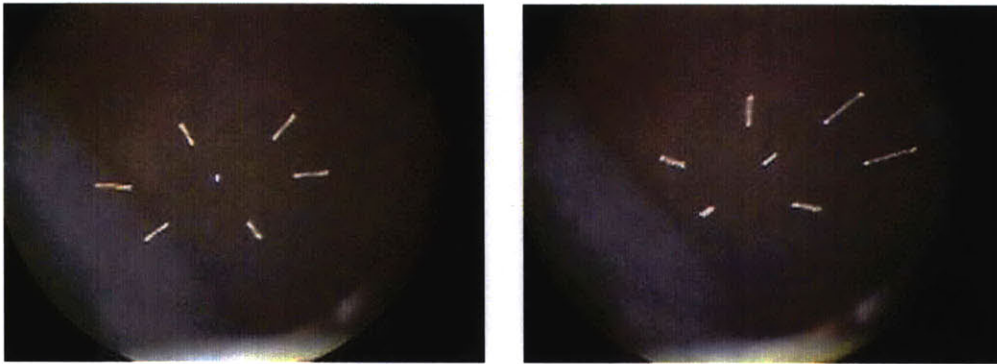


**Figure 4.5.** Demonstration trap suspending a Coulomb crystal of charged particles.

Figure 4.5 shows a common version of the Paul trap along with a Coulomb crystal structure consisting of 49 mutually repelling charged microspheres. The spheres appear as streaks because of their micromotion within the trap, and it can be seen that particles further from the equilibrium position (the trap center) have larger motion amplitude than those close to the center.

An extensive body of literature describes the application of linear quadrupole and hyperboloidal traps, particularly in the fields of mass spectrometry and aerosol microscopy[15][28]. Typically these techniques cancel the gravitational acceleration on a suspended sample by application of a static, homogenous electric field that balances the particle in the center of the trap and thus minimizes its micromotion.

By imaging a particle balanced in the plane of a hyperboloidal trap, one observes its amplitude of micromotion to depend on accelerations applied to the trap as well as gravitational acceleration, as discussed above. Furthermore, trapped many-body structures such as Coulomb or Wigner-Seitz “crystals” [31] – formed by the mutual repulsion of charged particles in a potential minimum – are known to demonstrate rigid-body dynamics, including conservation of angular momentum [16].

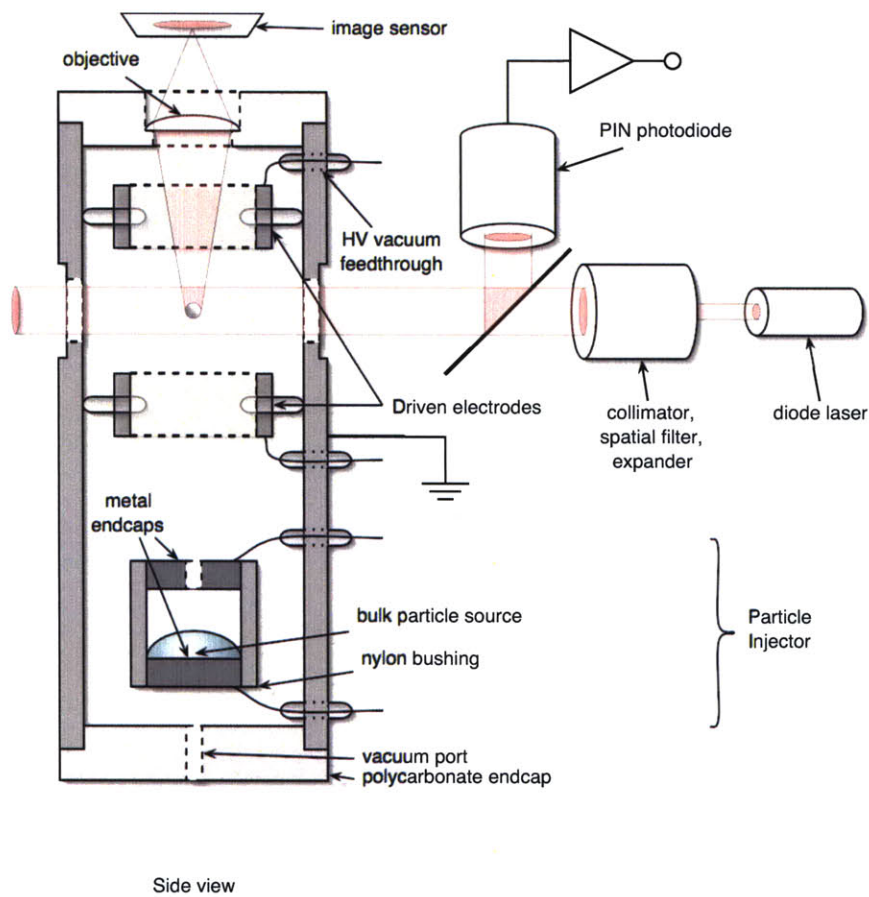


**Figure 4.6.** A Coulomb crystal of 7 charged particles in the  $z = 0$  trapping plane, without (left) and with (right) an acceleration applied in the plane.

Figure 4.6 shows the effect of an applied acceleration on particle micromotion. In the first

image, the central particle of a Coulomb crystal appears as a dot because it is at the equilibrium position, while the surrounding particles exhibit similar amounts of micromotion according to their similar displacements from the center. In the second image, the trap is accelerated toward the lower left corner of the image and the crystal is displaced from equilibrium. The central particle now appears as a streak, exhibiting a micromotion amplitude that corresponds to the applied amplitude.

### 4.3 Developing a practical trap



**Figure 4.7.** Schematic embodiment of an inertial measurement particle trap.

A typical experiment is detailed in Figure 4.7, embodying a design similar to those employed in

early studies of electrodynamically suspended particles [35]. To load the trap, a high-voltage step function is applied between the endcaps of the bulk particle source container, projecting inductively charged particles into the center of the trapping region where their motion is analyzed optically.

A diode laser and associated optics illuminate the trapping volume, which is projected onto a image sensor array. Backscattered light from the trapping volume is mixed with a fraction of the illuminating reference beam by a non-polarizing beam splitter and directed onto a photodiode detector. The resulting signal may be amplified, filtered, and integrated to provide interferometric readout of the particle's motion.

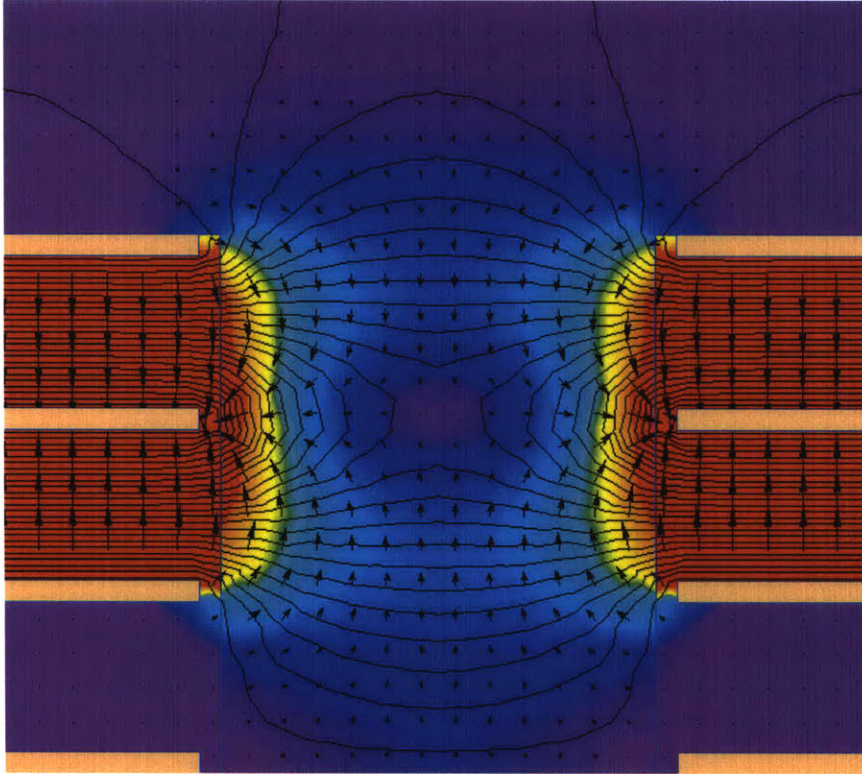
The actual trap consists of two driven ring electrodes while the grounded cylinder containing the entire assembly acts as a third, central ring electrode. The trapped particles are glass, metal, or liquid microspheres, anywhere from 0.1 to 100  $\mu\text{m}$  in diameter and charged to a few  $\mu\text{C}/\text{gm}$ . The active trapping volume is approximately  $1\text{ cm}^3$  and trapping voltages are on the order of 500 V to 5 kV, at frequencies from 50 Hz to 5000 Hz. A coherent collimated light source provides illumination for particles to be imaged on a CCD or CMOS camera. It also permits light scattered by particles to be mixed with a reference beam at a detector, allowing interferometric determination of the position at nanometer resolution.

The configuration shown in Figure 4.7 permits a great deal of flexibility in the development of experimental protocols, yet it fails to demonstrate the trap's viability as a micromachined sensor. Furthermore, a guiding principle of the experimental plan has been to simplify construction as much as possible – but not more so – relying on standard fabrication techniques.

Of the many variations on the hyperbolic geometry, the planar trap is most relevant. Its simplified geometry enables lithographic fabrication in micrometer dimensions, either individually or in arrays, and leads to “the possibility of ion-trap and integrated-circuit technology merging with a single chip containing the trap, diode lasers, and associated electronics.” [3] This is the direction in which we pursue development of an integrated, embeddable inertial sensor.

### 4.3.1 Planar traps

In the traps shown in Figures 4.5 and 4.7, the cylindrical symmetry of the Paul trap has been retained, and in particular the central ring electrode defining the radial trapping plane; however, the endcap electrodes have changed from hyperboloid shells to spherical shells and finally to rings. In the center of the trap, the field geometry is determined less by these particulars and more by the smoothing effect of the Laplacian operator acting upon the axially symmetric boundary conditions.



**Figure 4.8.** Finite-element calculation of field geometry in three-layer planar trap.

Figure 4.8 depicts the fields in a three-layer planar trap that has been fabricated as a printed circuit board. The structure is axisymmetric about the vertical centerline. The upper and lower electrodes are chosen to be the reference, while the central ring electrode is driven with an AC voltage to generate the trapping fields.

The electrostatic energy density is at a maximum at the edge of the driven electrode, and falls off to minima at the center and the periphery of the trap. Particles in the intermediate region will experience strong focusing effects that alternately push them towards and away from the center. The net effect is that particles with the correct charge-to-mass ratio  $e/m$  will be focused to the central region, just as with the canonical Paul trap. The central isoenergy surfaces in both cases are ellipsoidal, as details of the boundary geometry are smoothed out on the dipole length scale.

In the case where the fields are determined by a central electrode, with a ground reference supplied by a lower plane and a surrounding ring, the field geometry exhibits similar structure in the trap center. Figure 4.9 illustrates the situation: note that the isopotentials form a saddle as

before (albeit a warped saddle) but the isoenergy surfaces are clearly no longer closed.

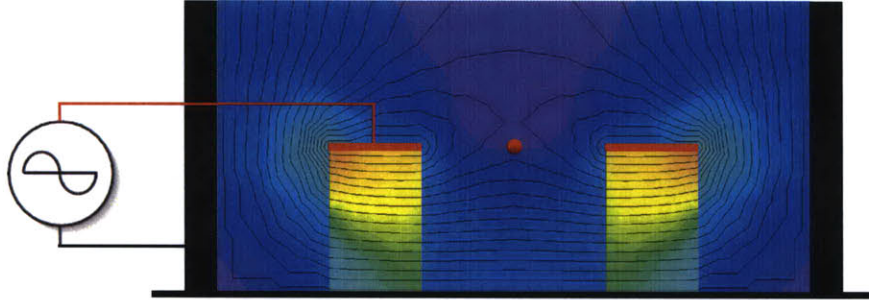


Figure 4.9. Finite-element calculation of field geometry in half-planar trap.

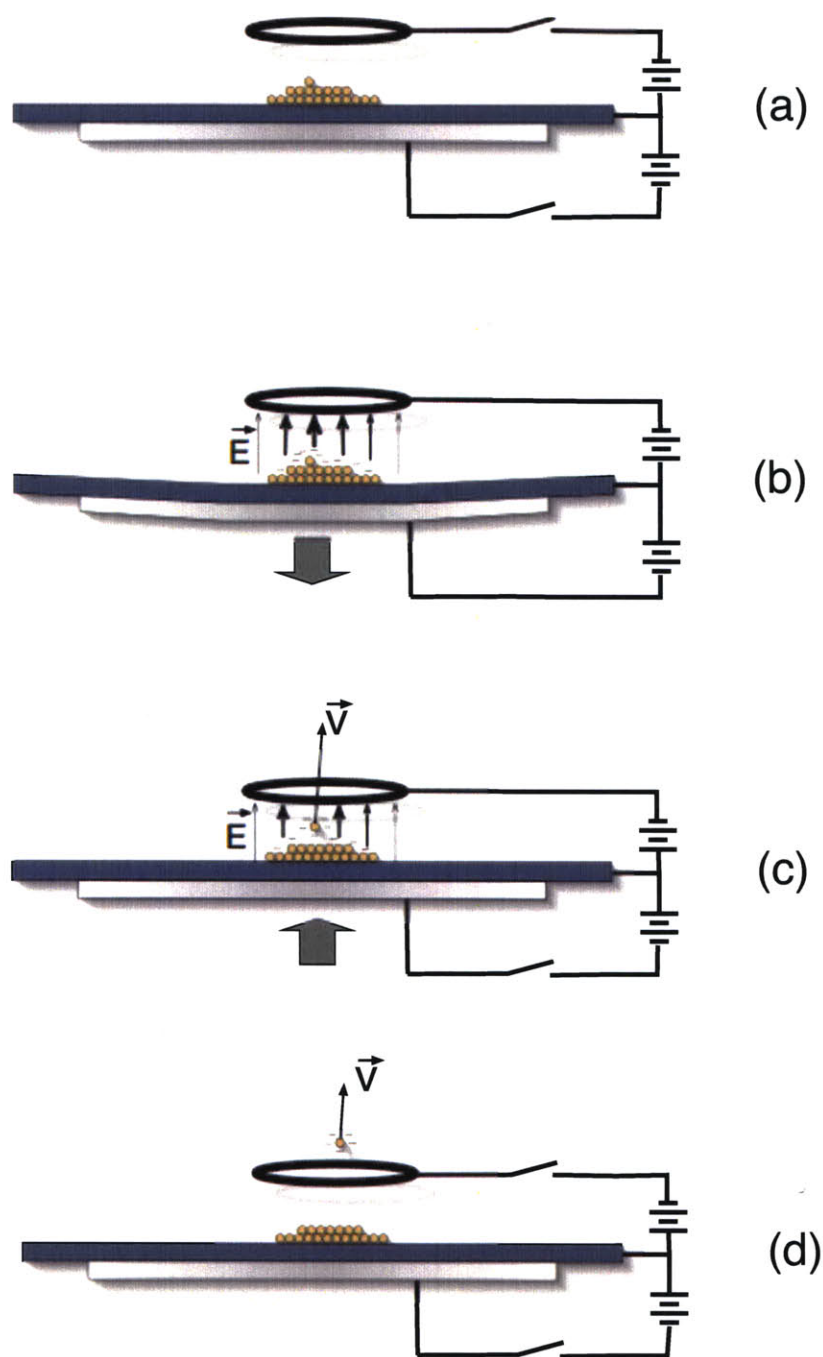
### 4.3.2 Trap loading

To demonstrate a working trap with particles of known mass and charge, one must be able to inject particles with known values of these quantities on demand. Since we are working with macroscopic particles with variable mass and geometry and bulk effects, this is not as simple as it may be in the case of ion traps. The literature of aerosol microscopy reveals a number of methods for particle charging and dispersal, but these require the use of conductive liquid media which we would rather avoid.

Ultimately it would be desirable to use proof mass particles with well-known charge and mass at low temperature, *e.g.*, ions of a naturally monoisotopic species ( $\text{Cs}^+$  comes to mind) forming an optically probed and cooled Wigner crystal.

For the experiments at hand, however, less exotic proof masses were chosen. Experiments were conducted with  $\mu\text{m}$ -scale spheres of borosilicate glass, aluminum, and gold. Gold particles were preferred because of their high density, low reactivity, and high conductivity. All experiments were performed using Au spheres with a mean diameter  $\bar{d} = 7.25 \mu\text{m}$  and standard deviation  $\sigma = 0.58 \mu\text{m}$ . At a density  $\rho_{\text{Au}} = 19300 \text{ kg} \cdot \text{m}^{-3}$ , these particles have an average mass  $\bar{m} = 3.85 \times 10^{-9} \text{ kg}$  (or 3.85 ng).

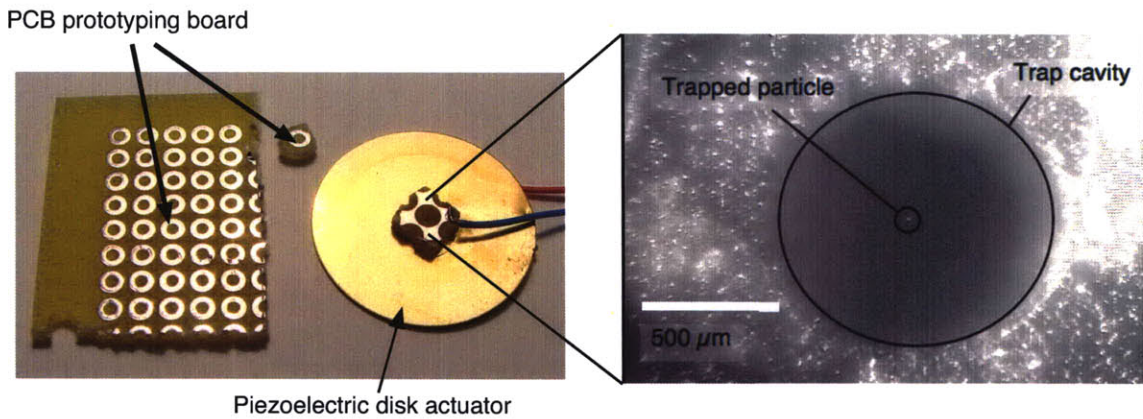
We solve the problem of charging and loading particles into the trap as shown in Figure 4.10. This technique is particularly applicable when the upper induction electrode also serves to generate the trapping field.



**Figure 4.10.** Trap loading and particle charging system in action. a) A granular bed of Au particles adheres to the conducting reference surface of a piezoelectric transducer. b) Voltage sources referenced to this surface are switched on to excite the piezoceramic and to generate an electric field. Charge redistributes on the conducting surface of the transducer and the adhered granular bed. c) The piezoceramic drive is switched off, the transducer relaxes, and a particle is ejected from the granular bed, carrying away charge. d) The induction ring electrode is switched off, allowing the particle to escape.

### 4.3.3 Planar trap construction

Putting together the above insights into trap planarization and loading, we construct a simple trap from common materials found in the electronics shop. Figure 4.11 shows the details of constructing a half-planar trap with a ring electrode (ID = 1.0mm,  $z_0 = 1.3$  mm,  $\epsilon_r \simeq 4.3$ ) from circuit prototyping board stock and a common acoustic piezotransducer. A high-voltage flying lead drives the central electrode while the brass disc of the transducer forms the common ground reference.



**Figure 4.11.** Construction detail of the half-planar trap ( $r \simeq 500\mu\text{m}$ ,  $z \simeq 1585\mu\text{m}$ ).

Finally the entire structure is surrounded by a grounded ring and mounted on a positioning stage as seen in Figure 4.12. The ring electrode is blackened with a permanent marker to enhance image contrast. A bubble level with resolution of 5 arcminutes is used to estimate horizontality, and an LED provides constant or synchronously strobed illumination for microscopic imaging.



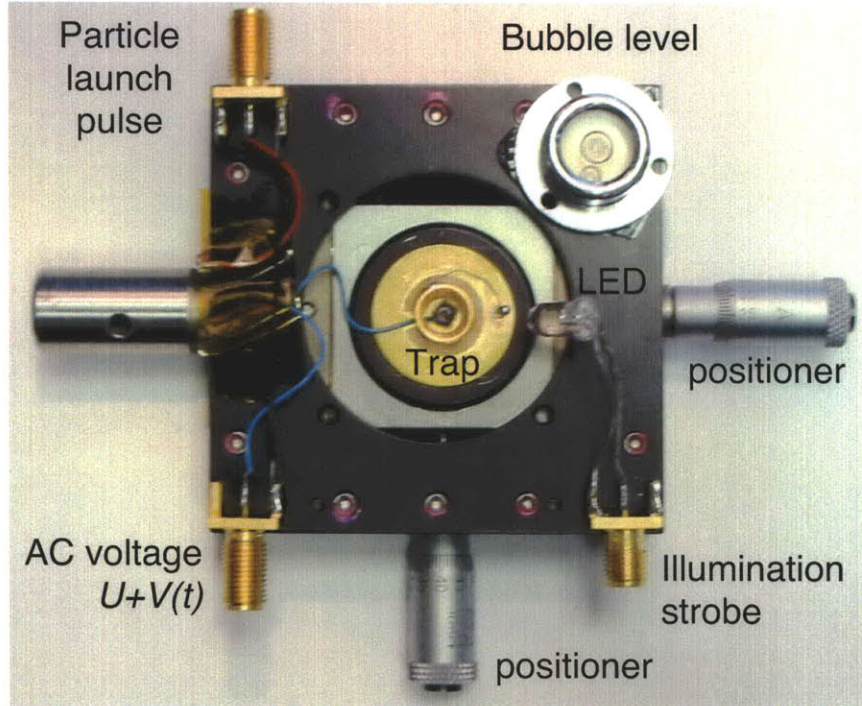


Figure 4.12. Detail of positionable planar trap module.

#### 4.3.4 Particle tracking and readout

Our sensor requires a readout of particle motion to permit determination of acceleration. Although the classic technique of ion trap mass spectroscopy [9][10] employs resonant absorption of radiofrequency energy to determine trap loading, this is too coarse a measure for our requirements. We require knowledge of the particle's position and breadth of motion from cycle to cycle of the trapping frequency. Capacitive particle position readout techniques are ruled out because they would require distinguishing small capacitive variations (on the order of  $10^{-15}$  F) in a large background (100V to 1000V).

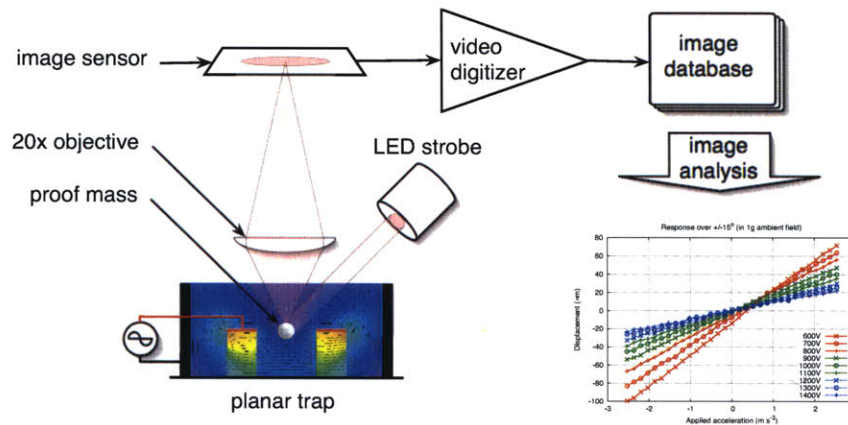
Optical readout techniques are more accessible and couple minimally to the large trapping field. Optical levers have been employed in many sensitive experiments, and have been shown to give resolution to 10 nm or better [33], while interferometric techniques can typically resolve motion to

1 nm or better [36]. However, optical levers are typically employed when the motion of interest is small, while interferometry is typically limited to scattering apertures incommensurate with the probe wavelength.

Since our present experimental techniques are performed without a closed control loop, large excursions are expected and the use of optical leverage becomes more complicated. As the particles of interest are spheres a few microns in diameter, their coherent scattering profiles significantly complicate the interpretation of interference fringes to determine position [13].

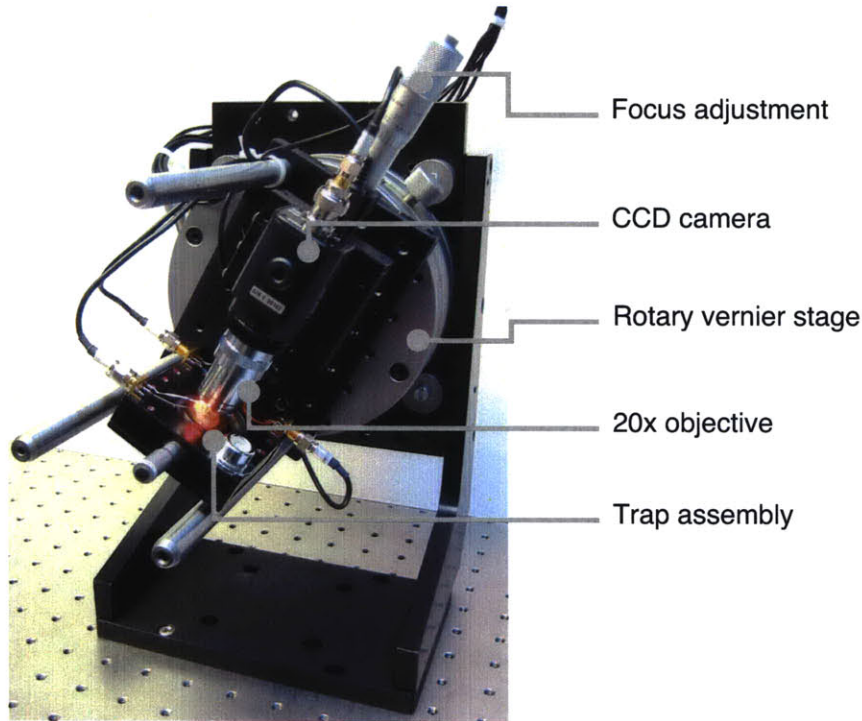
By relaxing the temporal and spatial resolution requirements, we can choose to employ video microscopy particle tracking, which is typically capable of locating submicron ( $> 200$  nm) spheres to within 10 nm in the focal plane and 150 nm in depth [8]. When information from individual images are combined into time series of single-particle trajectories it becomes possible to measure rheological parameters such as diffusion coefficients and pair-wise interaction potentials [12].

## 4.4 Experimental configurations



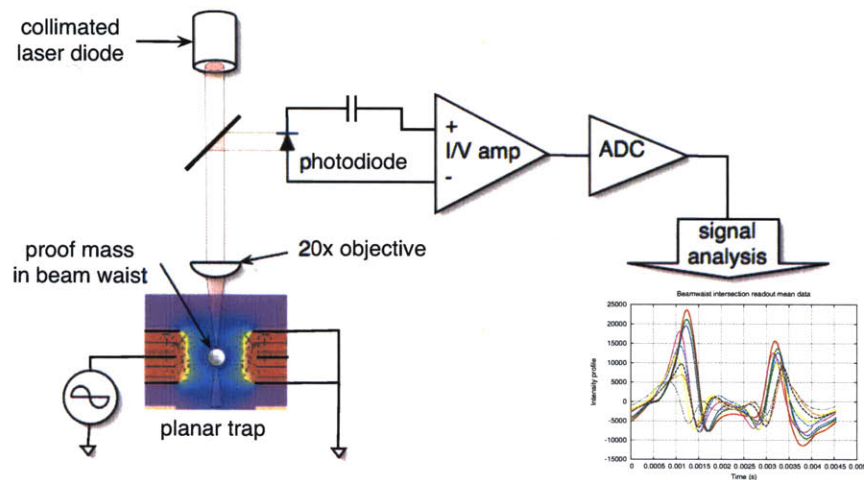
**Figure 4.13.** Experimental configuration for characterization by video microscopy.

Putting these details together we arrive at the experimental configuration shown in Figure 4.13. An LED illuminates the trap center, and particles therein are imaged by a microscope objective directly onto a CCD imaging array. The video signal is digitized into individually tagged frames that together constitute a database. This database is then processed offline to recover particle motion and other variables of interest. Finally, Figure 4.14 shows the physical apparatus embodying this configuration.



**Figure 4.14.** Experimental apparatus for characterization by video microscopy.

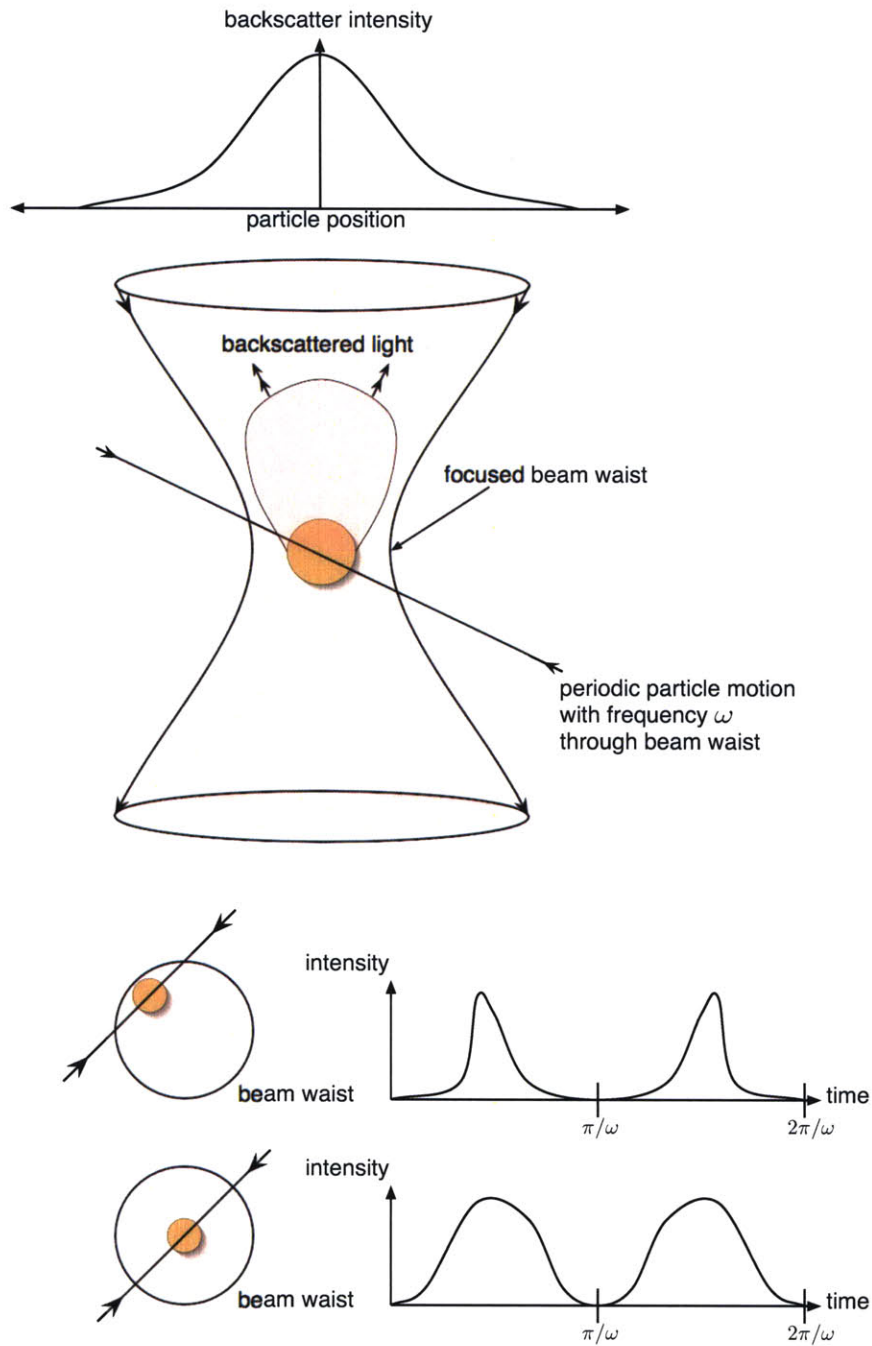
While this is a simple yet versatile system for trap characterization, readout bandwidth will be limited by the video frame rate to a fraction of the trapping frequency. Figure 4.15 shows an alternate configuration that may be used to measure small variations in particle position by a technique we propose as a variation on the optical lever.



**Figure 4.15.** Experimental configuration for measuring spectral noise density.

In this configuration we measure the intensity of light scattered by a particle as it moves through

the waist formed by a focused beam. This readout allows us to probe the spectral characteristics of trapped particle motion, and may be calibrated to provide an estimate of the scale of these effects.



**Figure 4.16.** Detail of beam waist intersection readout.

Finally, Figure 4.16 shows a plan detail of the beam waist readout. As a particle moves through the waist of a focused beam of light, it scatters light back into the focal cone. The observed backscatter depends on the intensity profile of the beam (*e.g.*, a diffraction-limited Gaussian), the scattering form factor of the particle, and the position of the particle as it moves through the beam.

If we assume that the particle's motion is harmonic, then the time-domain intensity profile will appear as a symmetric positive function. It is apparent that the intensity profile will depend on the center of motion, and as the center of motion moves toward the center of the beam we expect the intensity profile to widen or increase its duty cycle. Unfortunately, this effect will be complicated by motion parallel to the beam axis, so we consider it to be a rough diagnostic suitable for the measurement of small motions.

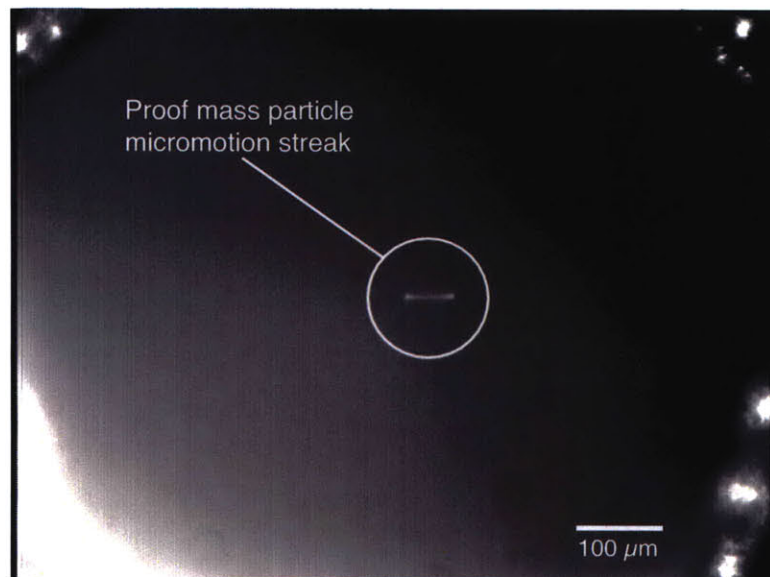


# Chapter 5

## Results

Our goal is to characterize the trap's response to acceleration. In the case of video microscopy, readout is performed by determining the particle's motion parameters from images of its activity in the trap. Center of motion was chosen as the readout statistic, but amplitude of micromotion could also be used.

A typical image of a single particle suspended in a trap is shown in Figure 5.1, with a particle suspended in the center of a 1 mm trapping cavity. In the image's corners the surface of the driven electrode is visible. While the particle is spherical with a nominal  $7.25\ \mu\text{m}$  diameter, it appears as a streak in this image due to micromotion.



**Figure 5.1.** Sample raw image from video microscope.

The spot function of the particle image is taken to be Gaussian as it moves harmonically in the pseudopotential. The cycle average of  $s(x)$  (the pixel value at position  $x$  in the image) has the form

$$\langle s_{\sigma, A, \omega, x_0}(x) \rangle = \frac{1}{\sqrt{2\pi\sigma}} \int_0^{2\pi/\omega} e^{-\frac{1}{2\sigma}[(x-x_0) - A \cos \omega t]^2} dt \quad (5.1)$$

where  $\sigma$  is the width of the particle's spot function and  $A$ ,  $\omega$ ,  $x_0$  are the particle's micromotion amplitude, frequency and center of motion respectively.

When numerically evaluated, this averaged spot function closely corresponds to the observed image intensity. However, the lack of a closed-form solution for this integral and the computational expense of its evaluation leads us to restrict attention to the center of motion statistic, which is determined quite simply as the first moment of the pixel intensity.

Readout bandwidth is fundamentally limited by the trapping frequency (in this work, typically 100 Hz to 10 kHz) because the pseudopotential is an average effect. In the case of video microscopy, readout is also band-limited by the video frame rate (here 30 Hz). We must be mindful of the effects of frequency aliasing in readout of particle motion, but as the particle is strongly damped (*i.e.*, it has a low Reynolds number) these effects are expected to be more pronounced with respect to the frame frequency than the trap frequency.

Here, we will restrict the use of video characterization to low-frequency effects (*e.g.*, static acceleration response) and use the alternate readout method of beam waist intersection to study response over larger bandwidths.

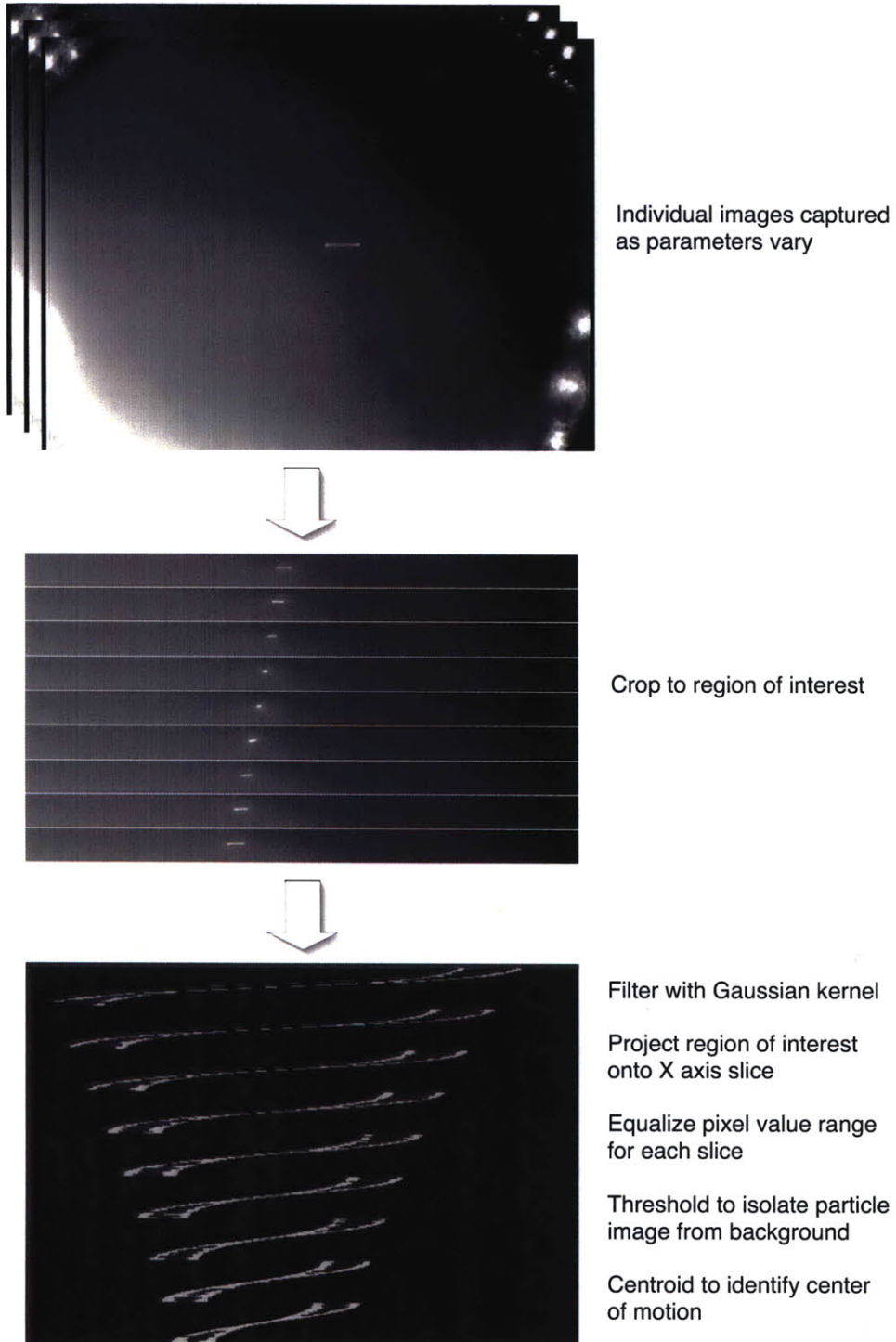
## 5.1 Experimental protocol

An experimental protocol was developed to accommodate the uncertainties in particle charge and mass. A candidate particle was identified and stabilized in the trap by a sweep through the full range of parameters to be varied in an experiment. Specific lateral accelerations  $a$  were applied as projections of the Earth's gravitational acceleration  $g$  by rotating the entire trap to an angle  $\theta$  in the Earth's gravitational field ( $a = g \sin \theta$ ). For small angles this corresponds to applied accelerations of approximately 17.4 mg/degree of rotation from the vertical.

Data were collected as series of images corresponding to variations in the independent variables of interest for each study. The imager employed was a Watec LCL-903K 1/3" monochrome CCD camera. The analog video signal from the camera was digitized by a Hauppauge WinTV tuner and video capture board. Images were captured using the `xawtv` utility and the `v4l` video-for-Linux



drivers running on a Linux 2.4.20 kernel. `xawtv` can be used to capture video frames with or without compression. Images captured for this study were uncompressed except where noted.



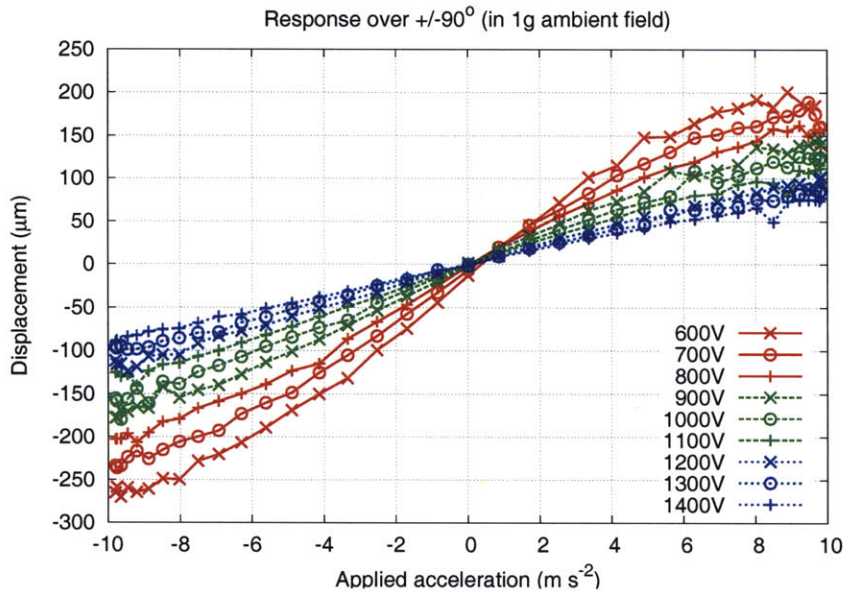
**Figure 5.2.** Image processing flow to reduce video microscopy data to particle motion parameters.

Once the images were captured and tagged with their acquisition parameters (trap voltage, frequency, *etc.*) they were processed to recover the particle motion parameters. Figure 5.2 illustrates the flow of data. Individual images of particle motion were cropped to the region of interest to reduce storage and processing requirements (as well as background noise). These cropped images were then convolved with a Gaussian kernel chosen to subtract the background and enhance features on the scale of the particle image [8].

The filtered, cropped images were then projected onto their long axis to create a single “slice” that captures particles’ motion along the axis of interest. Each slice was then equalized to maximize image contrast. A hard threshold was applied to distinguish particles from background. Finally, a centroid (first moment) operator was applied to obtain the center of particle motion.

## 5.2 Calibration

While it is not possible to determine the trap calibration *a priori* because of uncertainties in charge and mass (as well as geometric correction factors), the trap may be calibrated by applying known accelerations and measuring the response in terms of displacement of particle center of motion. This procedure may be repeated as trap parameters vary, allowing one to probe the tunability of trap response.



**Figure 5.3.** Calibration curve for displacement *vs.* acceleration.

Figure 5.3 shows the results of calibrating the trap as applied lateral acceleration varies from  $-1g$  to  $+1g$ . The trapping voltage was also varied, and as one would expect the response in displacement is greater for weaker trapping fields. Less expected is the apparent linearity of response over a fairly large central region of the trap.

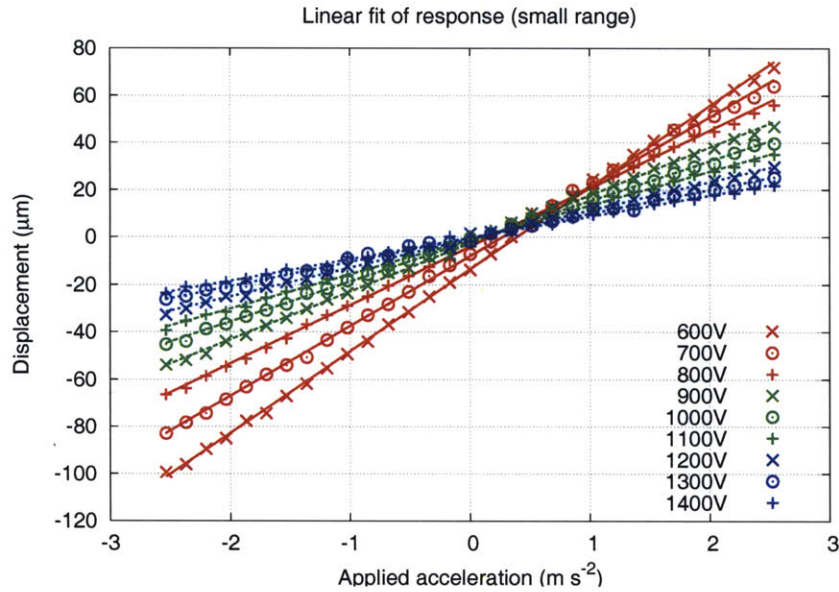


Figure 5.4. Calibration curve for displacement *vs.* acceleration, reduced range.

Figure 5.4 shows results that concentrating on the central linear region. Data points are plotted and a linear fit is drawn for each set. A good fit is observed, but to quantify this we plot the residual error of the fit in Figure 5.5.

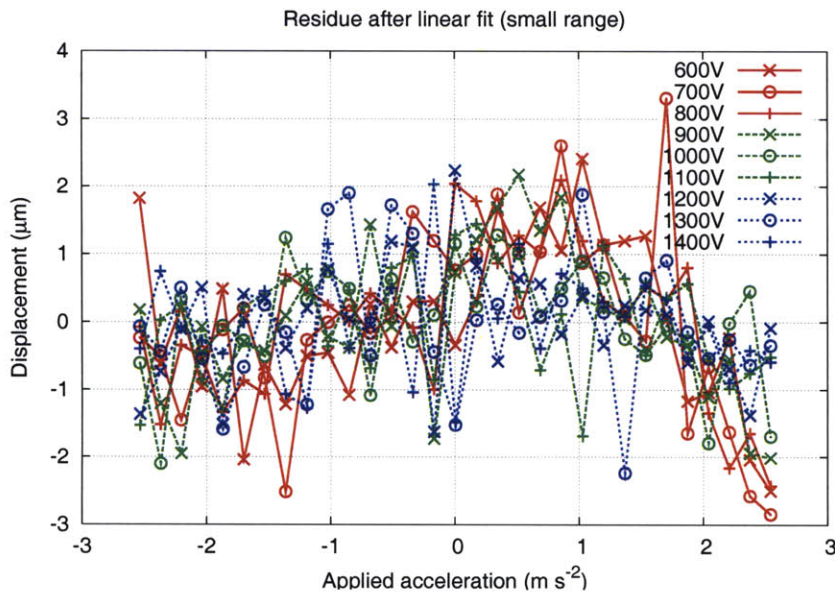
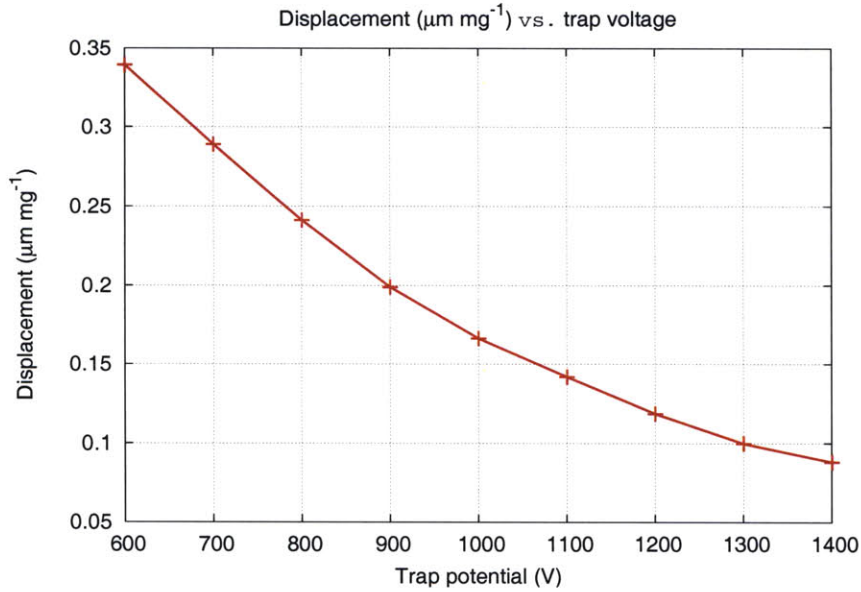


Figure 5.5. Residual error after linear fit.

### 5.3 Tunability

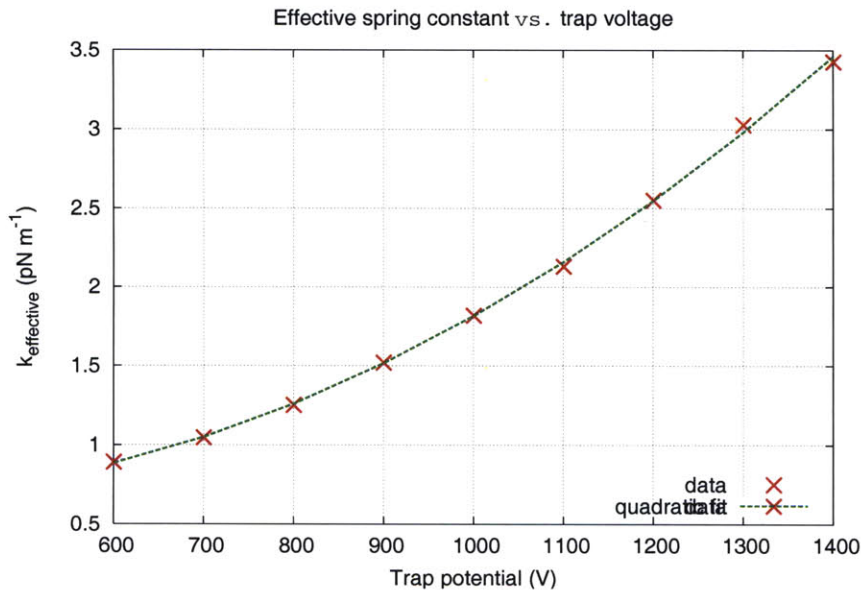
A unique feature of the inertial mode trap is its dynamic tunability or dependence of effective spring

constant  $\kappa = e^2 V^2 / m \omega_0^2 a_0^4$  on trap voltage and frequency. When the trap's linearized response is plotted against the trap voltage, the expected quadratic characteristic emerges.



**Figure 5.6.** Calibration constant *vs.* trap voltage.

This relationship is suggested by the  $1/\kappa$  dependence seen in Figure 5.6 and evidenced by a close quadratic fit of the measured effective spring constant, as shown in Figure 5.7. Here we have used the small-angle linearization (Figure 5.4) on the assumption that practical traps will be operated in the linear region with closed-loop control.

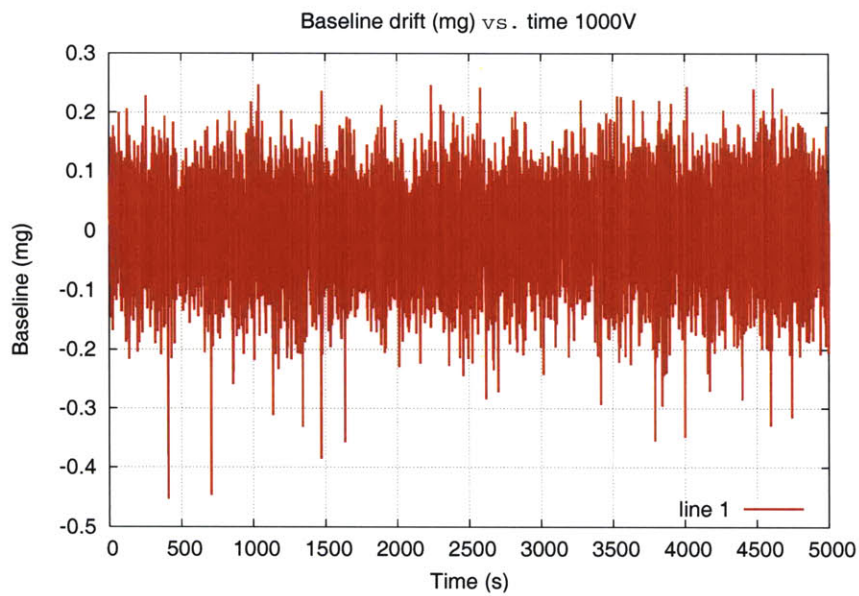


**Figure 5.7.** Effective spring constant *vs.* trap voltage.

## 5.4 Drift

Long-term variations in readout bias may also be observed by processing a time series of images. After data sets were collected for the above characterizations, the trap voltage was set to a midrange value of 1.0kV and the trap rotated to an angle of  $45^\circ$ , corresponding to an acceleration bias of  $0.707g$ .

Images of the particle were captured for 5000 seconds at a rate of 2 frames per second and the particle motion was determined through the same image processing chain as above. Variations in the center of motion were then plotted according to the above calibrations. Figure 5.8 shows the results of this measurement.

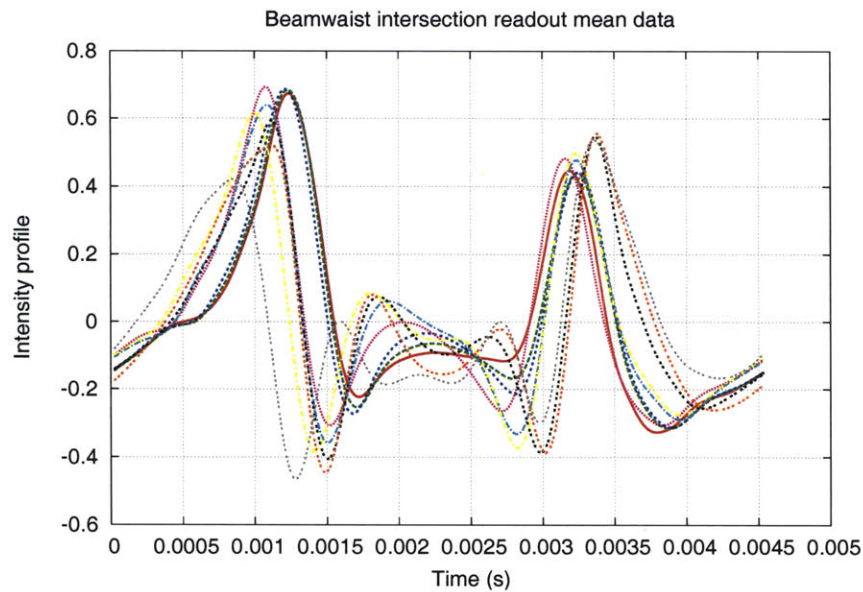


**Figure 5.8.** Baseline drift *vs.* time, sampled at 2 Hz.

The power spectral density of this measurement is flat up to 1 Hz (half the sampling frequency), suggesting that the measurement error exceeds the trap's intrinsic physical noise from sources such as Brownian motion or fluctuation-dissipation.

## 5.5 Noise power spectral density

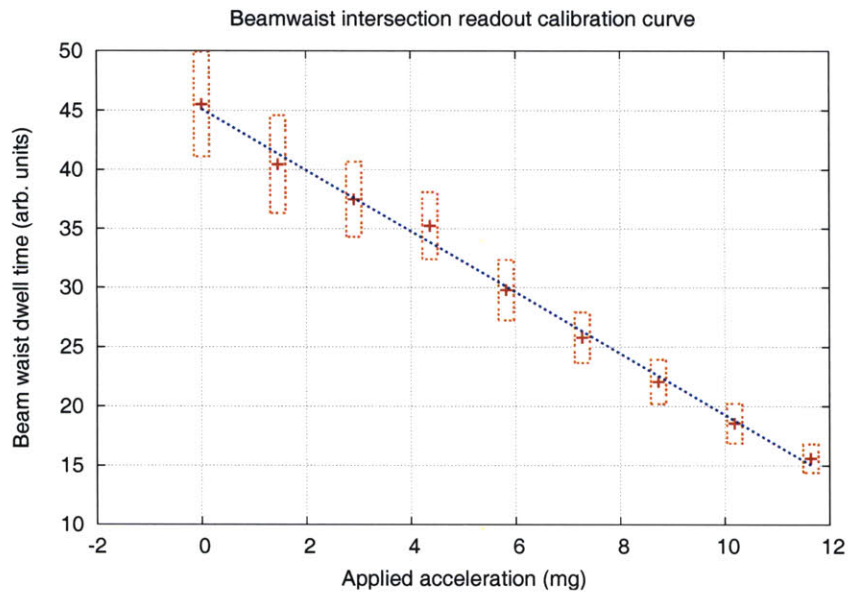
To probe the noise structure intrinsic to our accelerometer, we turn to an alternate experimental configuration utilizing readout of the beam waist intersection. This measurement was calibrated by applying known small accelerations and recording long time series of scattering intensity. Typical time-domain profiles of scattering intensity are shown in Figure 5.9.



**Figure 5.9.** Mean intensity profiles of beam waist intersection for varying applied acceleration.

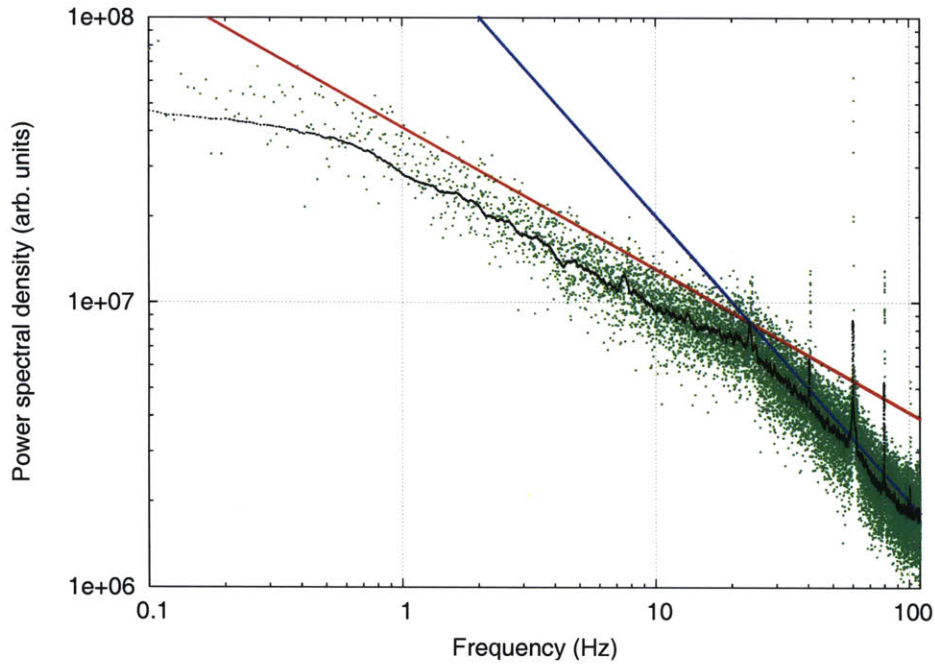
Here, the trap operated at 1.1 kV and 220.5 Hz, and the curves shown each correspond to a different applied acceleration. Each curve is the mean profile obtained by phase-coherent averaging of 25,000 samples. As we showed before, one might expect the observed widening of these profiles to correspond to an increased intersection of the particle with the beam waist.

This widening can be recovered by taking as a statistic the (centered) second moment of the intensity profile. We call the square root of the second moment the beam waist dwell time and plot this against applied acceleration in Figure 5.10 as a calibration curve. Over the small range of variations involved ( $\sim 10$  mg) we are rewarded by observing a reasonably linear response.



**Figure 5.10.** Beamwaist intersection readout calibration curve.

Because this measurement compresses several degrees of motional freedom into one and the beam waist geometry is not well-known, it is difficult to estimate the absolute scale of these measurements. We can however reasonably conclude from this calibration curve that there are no strong nonlinearities lurking in our measurement, and begin to consider features of the noise spectral power density if not its absolute scale.



**Figure 5.11.** Power spectral density of beam waist drift measurement. A moving average of 55 samples is plotted over the field of data points. Solid lines provide scaled references for  $1/f$  and  $\sqrt{1/f}$  trends.

Figure 5.11 shows the power spectral density of the same data used to obtain the calibration curve. Dots are plotted for individual points in the density along with a moving average of 50 points to accentuate features in the density. A peak at 23.7 Hz coincides with an apparent shift in the noise density trend from  $f^{-1/2}$  to  $f^{-1}$  (solid lines). A very strong peak appears at 60 Hz as one might expect, but peaks also appear at 43.5 Hz, 80.0 Hz, and 100 Hz. The graph cuts off at 110.25 Hz, half the trapping frequency.



# Chapter 6

## Discussion

First, a brief note about contributions made in this dissertation.

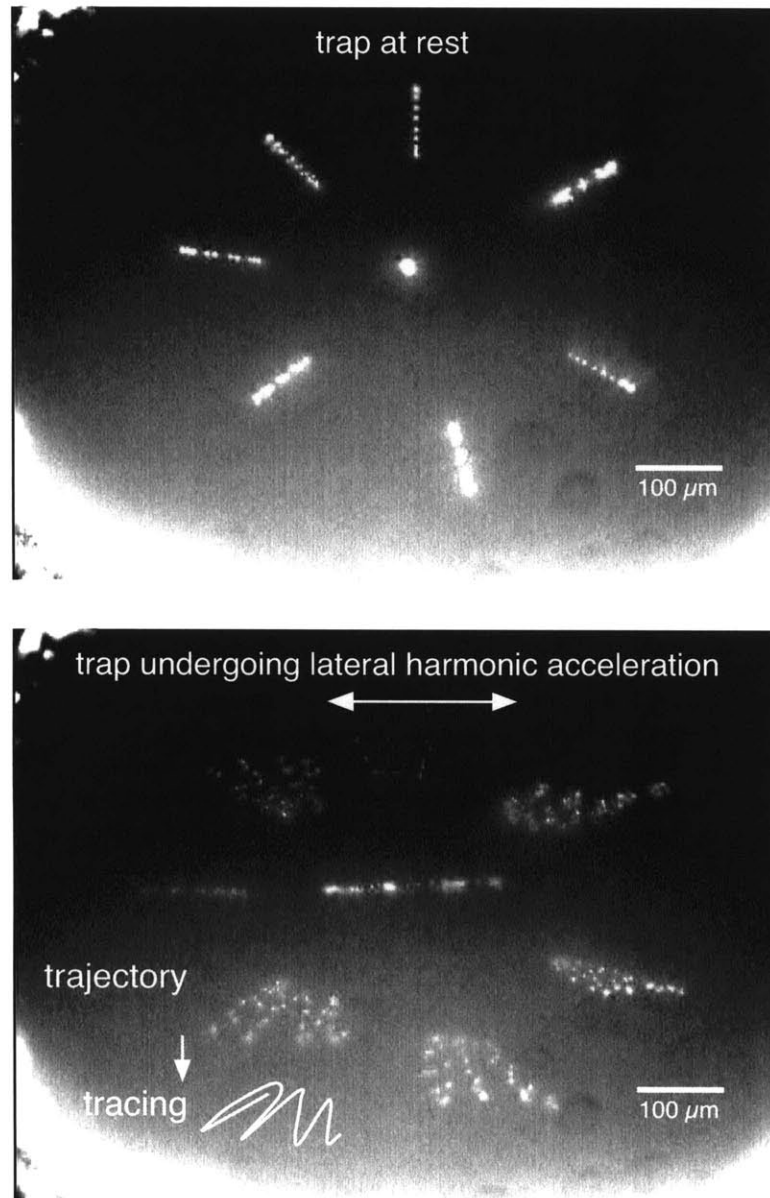
We believe that this work has for the first time developed and demonstrated the theory and practice of inertial measurement using an electrostatically levitated proof mass. Specifically, by adding inertial terms to the Paul trap dynamics we have derived classical observables that depend on the local acceleration field.

We have also confirmed that these observables appear in practice, in what we believe to be the first electrodynamic trap accelerometer. An important (and unusual) aspect of our accelerometer is its dynamic tunability: its effective spring constant depends on the trap drive parameters. Our roughly constructed trap exhibits a large region of linear response to acceleration and we have presented evidence to suggest that the total noise power in typical operation of the trap lies below a readout noise floor of  $\sim 0.2\text{mg}$ .

### 6.1 Future work

All of the traps used in this work were hand-crafted, leading to uncertainties in size, shape, planarity, dielectric distribution, and symmetry. By fabricating traps on printed circuit boards (PCBs) we expect to achieve tighter control over these physical trap parameters, as well as a much more compact package than the experimental apparatus used in this work. This will greatly simplify the fixturing and characterization of traps. Our current experiments are not suitable to studies of trap frequency response because the apparatus hosts numerous mechanical resonances within the bands of interest.

The next step would be to simplify metrology. Two leading candidates are self-mixing laser diode velocimetry (SMLDV) [19][29] and differential optical leverage [33]. SMLDV might be accomplished simply by mounting a laser diode sufficiently close to the trap that scattering from the particle influences mode selection in the laser diode [21] – in other words, the particle effectively becomes a mirror defining a Fabry-Perot cavity external to the laser diode package. Most laser diodes are packaged with a photodiode used for optical feedback mode locking; the signal from this photodiode may also be used to observe laser intensity variations (due to the action of the external cavity) analogous to the interference fringes that occur in a Michelson interferometer [?]. By placing several of these SMLDV sensors to track a particle along non-parallel axes, we might expect to recover the particle’s three-dimensional motion by triangulation or orthogonalization of the combined interferometric signals.



**Figure 6.1.** Trapped Coulomb crystal of Au particles at rest and harmonically accelerated at 210 Hz. Trapping at  $V = 1.0$  kV,  $\omega_0 = 240$  Hz. Illumination strobe at 2400 Hz.

We have observed Coulomb crystals in traps both large [28] and small. In Figure 6.1 we demonstrate the lateral inertial excitation of a Coulomb crystal. Trajectories appear discrete because particles are stroboscopically illuminated. One of these trajectories has been manually traced to clarify its form. This trajectory – essentially a 3-dimensional Lissajous pattern – holds a wealth of information about the trapping fields, the applied acceleration, and the timing of these events. It is the goal of future work to tease this information out of the system with simplified metrological techniques.

We also observe that these harmonically accelerated crystals to be stable for tens of hours. The crystal shown above, for example, remained stable under this applied excitation for over 30 hours, at which point the experiment was interrupted.

Interestingly enough, this crystal maintained its orientation in the trap throughout the experiment, although we expected to observe some net rotational drift by the end. Several reasons for this (undesired) stabilization come to mind: trap electrode asymmetry might have been sufficient to strongly define a preferred orientation; charge accumulation on the trap might also play a role; or perhaps it is strong viscous damping due to the atmosphere in this  $1\text{ mm}^3$  trap cell. We hope to better determine the cause of this orientation to allow us to either a) free the crystal to rotate or b) better understand the effective torque keeping the crystal oriented.

Our trap loading mechanism points to a wealth of follow-on work. Particle mass and charge are not well-known with the current loading protocol, but could be better determined by using the trap in a spectroscopic mode to determine the particle's  $e/m$  ratio [35]. If massive (micron-scale) particles are to be used they must be stored when the trap is not operating, in such a way as to maintain their integrity.

One might even consider the use of crystallized plasmas [31] as proof masses. Such structures are amenable to sensitive optical probes such as Bragg scattering [16] to determine lattice parameters and also exhibit rigid body dynamics.

Simplified optical metrology has been mentioned, but we might even consider using the beam waist intersection readout to measure small motions in a trap operating under closed-loop control. Such a trap might have a more versatile electrode geometry [20] than those used in the present work to permit force balancing or the current trap might be operated in a mode where the spring constant is continuously retuned to keep the proof mass in a small measurement zone.

Finally, there is the matter of agile high-voltage control. In the course of this work we have pushed our operating voltages from 6 kV down to 600 V (and as low as 200 V in some cases not documented here). While it is important to identify ways to push the operating voltage lower still, we must also develop or identify a means to drive small capacitive loads with good phase control at frequencies from 50 Hz to 5 kHz and voltages up to 1 kV. Ideally, this high-voltage signal generator could be controlled by a microprocessor and fit within  $1\text{ cm}^3$ .



# Bibliography

- [1] ANALOG DEVICES. *Low Cost  $\pm 2g/\pm 10g$  Dual Axis iMEMS Accelerometers with Digital Output*. Norwood, Massachusetts, 1999. ADXL202/ADXL210 product datasheet.
- [2] ARNDT, M., AND ZEILINGER, A. Wave-particle duality of  $C_{60}$ . *Nature* *401* (14 October 1999), 680–682.
- [3] BREWER, R. G., DEVOE, R. G., AND KALLENBACH, R. Planar ion microtraps. *Phys. Rev. A* *46*, 11 (December 1992), R6781–R6784.
- [4] CHANG, A., RESNER, B., KOERNER, B., WANG, X., AND ISHII, H. Lumitouch: An emotional communication device. In *Extended Abstracts of Conference on Human Factors in Computing Systems (CHI '01)* (Seattle, Washington, March 31 - April 5 2001), CHI, ACM Press, pp. 313–314.
- [5] CHECKA, N. A system for tracking and characterizing acoustic impacts on large interactive surfaces. Master's thesis, Massachusetts Institute of Technology, May 2001.
- [6] CHU, S. The manipulation of neutral particles. *Reviews of Modern Physics* *3*, 70 (July 1998), 685–706.
- [7] COOPER, E. B., POST, E. R., GRIFFITH, S., LEVITAN, J., MANALIS, S. R., SCHMIDT, M. A., AND QUATE, C. F. High-resolution micromachined interferometric accelerometer. *Applied Physics Letters* *76*, 22 (29 May 2000), 3316–3318.
- [8] CROCKER, J., AND GRIER, D. Methods of digital video microscopy for colloidal studies. *Journal of Colloidal Interface Science* *179* (1996), 298–310.
- [9] DEHMELT, H. G. Radiofrequency spectroscopy of stored ions I: Storage. In *Advances in Atomic and Molecular Physics*, Bates and Estermann, Eds., vol. 3. Academic Press, New York, 1967, pp. 53–72.
- [10] DEHMELT, H. G. Radiofrequency spectroscopy of stored ions II: Spectroscopy. In *Advances in Atomic and Molecular Physics*, Bates and Estermann, Eds., vol. 5. Academic Press, New York, 1969, pp. 109–154.
- [11] DEVOE, R. G. Elliptical ion traps and trap arrays for quantum computation. *Phys. Rev. A* *58*, 2 (August 1998), 910–914.
- [12] GARDEL, M. L., VALENTINE, M. T., AND WEITZ, D. A. Microrheology. In *Microscale Diagnostic Techniques*, K. Breuer, Ed. Springer Verlag, 2002.
- [13] GOODMAN, J. W. *Introduction to Fourier Optics*. McGraw-Hill Science/Engineering/Math, 1996.
- [14] HINCKLEY, K., PIERCE, J., SINCLAIR, M., AND HORVITZ, E. Sensing techniques for mobile interaction. In *ACM UIST 2000 Symposium on User Interface Software and Technology* (2000), CHI Letters 2 (2), ACM Press, pp. 91–100.
- [15] HOFFNAGLE, J., AND BREWER, R. G. Frequency-locked motion of two particles in a Paul trap. *Physical Review Letters* *71*, 12 (20 September 1993), 1828–1831.
- [16] HUANG, X.-P., BOLLINGER, J. J., MITCHELL, T. B., AND ITANO, W. M. Phase-locked rotation of crystallized non-neutral plasmas by totating electric fields. *Phys. Rev. Lett.* *80* (1998), 73–76.

- [17] ISHII, H., WISNESKI, C., ORBANES, J., CHUN, B., AND PARADISO, J. Pingpongplus: Design of an athletic-tangible interface for computer-supported cooperative play. In *Conference on Human Factors in Computing Systems* (May 15-20 1999), SIGCHI '99, ACM Press, pp. 394–401.
- [18] J. J. SAKURAI, S. F. T. *Modern Quantum Mechanics*, 2 ed. Addison-Wesley, 1994.
- [19] KAWAI, R., ASAKAWA, Y., AND OTSUKA, K. Ultrahigh-sensitivity self-mixing laser doppler velocimetry with laser-diode-pumped microchip  $\text{LiNdP}_4\text{O}_{12}$  lasers. *IEEE Photonics Tech. Lett.* 11, 6 (June 1999), 706–708.
- [20] KIELPINSKI, D., MONROE, C., AND WINELAND, D. J. Architecture for a large-scale ion-trap quantum computer. *Nature* 417 (June 2002), 709–711.
- [21] LANG, R., AND KOBAYASHI, K. External optical feedback effects on semiconductor injection laser properties. *IEEE Journal of Quantum Electronics QE-16*, 3 (March 1980), 347–355.
- [22] LOH, N. C., SCHMIDT, M. A., AND MANALIS, S. R. Sub- $10\text{cm}^3$  interferometric accelerometer with nanog resolution. *Journal of Microelectromechanical Systems* 11, 3 (June 2002), 182–187.
- [23] MCLEOD, D. L. Miniaturization of the solid rotor electrostatic gyro. In *IEEE Proc. National Aerospace and Electronics Conference (NAECON) part III* (1979), IEEE, pp. 1199–1205.
- [24] MICHELSON, A. A. *Studies in optics*. University of Chicago Press, 1962.
- [25] PARADISO, J. Responsive window. In *Takeover - Proceeding of Ars Electronica* (Vienna/New York, 2001), Springer, pp. 261–263.
- [26] PAUL, W. Electromagnetic traps for charged and neutral particles. *Reviews of Modern Physics* 62, 3 (July 1990), 531–540.
- [27] PRESS, W. H., TEUKOLSKY, S. A., VETTERLING, W. T., AND FLANNERY, B. P. *Numerical Recipes in C: The Art of Scientific Computing*, 2nd ed. Cambridge University Press, New York, 1992.
- [28] ROBERTSON, S., AND YOUNGER, R. Coulomb crystals of oil droplets. *American Journal of Physics* 67, 4 (April 1999), 310–315.
- [29] SHIBATO, T., SHINOHARA, S., IKEDA, H., YOSHIDA, H., SAWAKI, T., AND SUMI, M. Laser speckle velocimeter using self-mixing laser diode. *IEEE Trans. on Inst. and Meas.* 45, 2 (April 1996), 499–504.
- [30] STROGATZ, S. *Nonlinear Dynamics and Chaos*. Perseus Publishing, Cambridge, Massachusetts, 1994.
- [31] TAN, J. N., BOLLINGER, J. J., JELENKOVIC, B., AND WINELAND, D. J. Long-range order in laser-cooled, atomic-ion Wigner crystals observed by Bragg scattering. *Phys. Rev. Lett.* 75 (1995), 4198–4201.
- [32] VERPLAETSE, C. Inertial proprioceptive devices: Self-motion-sensing toys and tools. *IBM Systems Journal* 35, 3+4 (1996), 639–650.
- [33] VISSCHER, K., GROSS, S. P., AND BLOCK, S. M. Construction of multiple-beam optical traps with nanometer-resolution position sensing. *IEEE Journal of Selected Topics in Quantum Electronics* 2, 4 (December 1996), 1066–1076.
- [34] WEISER, M. The computer for the 21st century. *Scientific American* 265, 3 (September 1991), 94–104.
- [35] WUERKER, R. F., SHELTON, H., AND LANGMUIR, R. V. Electrodynamic containment of charged particles. *J. Appl. Phys.* 30 (1959), 342–349.
- [36] YARIV, A. *Optical Electronics*, 4th ed. Saunders College Pub., Philadelphia, 1991.